ENCLOSURE 2

FLN-2007-023

COBRAG Subchannel Code - Model Description Report, NEDE-32199P, Revision 1, July 2007

Non-Proprietary Information

IMPORTANT NOTICE

This is a non-proprietary version of Enclosure 1 to FLN-2007-023, which has the proprietary information removed. Portions of the document that have been removed are indicated by white space with an open and closed bracket as shown here [[ ]].

Global Nuclear Fuel

A Joint Venture of GE, Toshiba, & Hitachi

NEDO-32199
Revision 1
Class I
eDRF-0000-0062-7413
July 2007

Licensing Topical Report

COBRAG SUBCHANNEL CODE

MODEL DESCRIPTION REPORT

J. G. M. Andersen
R. Harrington
B. Hizoum

Legal Notice

This document was prepared by Global Nuclear Fuel (GNF). The use of this information for any purpose(s) other than that for which it is intended, is not authorized; and with respect to any unauthorized use, GNF makes no representation or warranty, expressed or implied, as to the completeness, accuracy, or usefulness of the information contained in this document, or that its use may not infringe privately owned rights, and assumes no responsibility for liability or damage of any kind that may result from such use of this information.

Information Notice

This is a non-proprietary version of the document NEDE-32199P, Revision 1, which has the proprietary information removed. Portions of the document that have been removed are indicated by an open and closed bracket as shown here [[ ]].

Document Title: COBRAG - Steady State Sub-Channel Analysis Code

July 2007

ABSTRACT

COBRAG is a steady state subchannel analysis code for performing analysis on BWR or simulated BWR fuel bundles. It can be used to predict bundle critical powers and dryout locations, bundle planar averaged and local void fractions, and bundle pressure drops. This document provides a description of the physical models and numerical methods in COBRAG.

The subchannel two-phase flow is described by a two-fluid, multi-field model. Interactions between the fields are modeled through constitutive correlations for interfacial shear and heat transfer, entrainment and deposition. Inter-subchannel transport phenomena like mixing and void drift are also modeled. Energy transfer from the wall is modeled as a boundary condition. Physical models include a full or part length fuel rod model with its own specific axial power profile and peaking factor, and a semi-empirical spacer model.

COBRAG is capable of simulating a broad range of bundle geometries. Bundles with large water rods, part length rods, and full length rods can be modeled with their own specific size, axial power profile and local peaking. Bundle inlet and outlet conditions including inlet flow distribution are simulated as boundary conditions specified by the users.

Acknowledgments

This document is the result of the technical contributions from many individuals and organizations in addition to the authors of this document. Significant contributions to the development of COBRAG have been made by Md. Alamgir, K. H. Chu. The advice and careful review of this document from Birol Aktas is highly appreciated. Also, the work of F. Skipper in assembling and editing the document is gratefully appreciated.

Revisions Summary

Revision	Comments
0	Revision 0 is an internal document.
1	Revision 1 is an updated version of Revision 0 that is prepared and marked for submittal to the US NRC.

TABLE OF CONTENTS

TABLE OF CONTENTS

LIST OF FIGURES

LIST OF TABLES

1.0 INTRODUCTION

COBRAG is a Global Nuclear Fuel (GNF) proprietary version of COBRA (Coolant Boiling in Rod Arrays) [1]. It is a best estimate code for subchannel analysis of thermal–hydraulic phenomena in a BWR type fuel bundle.

1.1 Scope and Capabilities

COBRAG is a steady state subchannel analysis code for performing analysis on BWR or simulated BWR fuel bundles. It can be used to predict bundle critical powers and dryout locations, bundle planar averaged and local void fractions and bundle pressure drops.

The subchannel two–phase flow is described by a two–fluid, multi–field model. Interactions between the fields are modeled through constitutive correlations for interfacial shear and heat transfer, entrainment and deposition. Inter–subchannel transport phenomena like mixing and void drift are also modeled. Energy transfer from the wall is modeled as a boundary condition. Physical models include a full or part length fuel rod model with its own specific axial power profile and peaking factor, and a semi–empirical spacer model.

COBRAG is capable of simulating a broad range of bundle geometries. Bundles with large water rods, part length rods, and full length rods can be modeled with their own specific size, axial power profile and local peaking. Bundle inlet and outlet conditions including inlet flow distribution is simulated as boundary conditions specified by the users.

2.0 THERMAL HYDRAULIC MODEL

A three dimensional two–fluid and three–field model which is considered to be the most appropriate to provide the capability of describing the film dryout phenomenon, non–equilibrium effects and subchannel mixing, is adopted to model the two–phase flow. The two fluids represented are the vapor and liquid phases while the three fields represent the continuous vapor or bubbles, the continuous liquid or droplets, and the liquid film fields. The model is governed by the conservation equations of mass, momentum and energy for the two–phase flow.

In COBRAG, the governing equations of the two–phase flow model are the conservation equations in mass, momentum, and energy for each field. They are formulated as follows:

2.1 GOVERNING EQUATIONS AND ASSUMPTIONS

In COBRAG, the governing equations of the two–phase flow model are the conservation equations in mass, momentum and energy for each field. They are formulated as follows:

$$\frac{\partial}{\partial t}\left(\alpha_g \rho_g\right) + \nabla\bullet\left(\alpha_g \rho_g \vec{v}_g\right) = \Gamma_g + M_{mix,g} \tag{2.1-1}$$

Liquid mass:

$$\frac{\partial}{\partial t}\left(\alpha_e \rho_\ell\right) + \nabla\bullet\left(\alpha_e \rho_\ell \vec{v}_e\right) = -\Gamma_e + \sum_k \left(E_k - D_k\right) + M_{mix,e} \tag{2.1-2}$$

Liquid film mass:

$$\frac{\partial}{\partial t}\left(\alpha_{f,k} \rho_\ell\right) + \nabla\bullet\left(\alpha_{f,k} \rho_\ell \vec{v}_{f,k}\right) = -\Gamma_{f,k} + \left(D_k - E_k\right) + M_{fs,k} \tag{2.1-3}$$

Vapor momentum:

$$\frac{\partial}{\partial t}\left(\alpha_g \rho_g \vec{v}_g\right) + \nabla\bullet\left(\alpha_g \rho_g \vec{v}_g \vec{v}_g\right) = -\alpha_g \rho_g \vec{g} - \alpha_g \nabla P - \vec{F}_{ie} - \sum_k \vec{F}_{if,k} - \sum_k \vec{F}_{wg,k} + \vec{B}_{mix,g} + \vec{F}_{vd} \tag{2.1-4}$$

Liquid momentum:

$$\frac{\partial}{\partial t}\left(\alpha_e \rho_\ell \vec{v}_e\right) + \nabla\bullet\left(\alpha_e \rho_\ell \vec{v}_e \vec{v}_e\right) = -\alpha_e \rho_\ell \vec{g} - \alpha_e \nabla P + \vec{F}_{ie} - \sum_k \vec{F}_{we,k} + \vec{B}_{mix,e} - \vec{F}_{vd} + \sum_k \left(E_k \vec{v}_{f,k} - D_k \vec{v}_e\right) \tag{2.1-5}$$

Liquid film momentum:

$$\frac{\partial}{\partial t}\left(\alpha_{f,k}\rho_f \vec{v}_{f,k}\right) + \nabla\bullet\left(\alpha_{f,k}\rho_f \vec{v}_{f,k}\vec{v}_{f,k}\right) = -\alpha_{f,k}\rho_f \vec{g} - \alpha_{f,k}\nabla P + \vec{F}_{if} - \vec{F}_{wf,k} + \vec{B}_{fs,k} + \left(D_k \vec{v}_e - E_k \vec{v}_{f,k}\right) \quad (2.1\text{-}6)$$

Vapor energy:

$$\frac{\partial}{\partial t}\left(\alpha_g \rho_g h_g\right) + \nabla\bullet\left(\alpha_g \rho_g \vec{v}_g h_g\right) = \alpha_g \frac{\partial P}{\partial t} + \Gamma_g h_g + q_{ig} + \sum_k q_{wg,k} + E_{mix,g} \quad (2.1\text{-}7)$$

Total energy:

$$\frac{\partial}{\partial t}\left(\alpha_g \rho_g h_g + \alpha_e \rho_f h_f + \sum_k \alpha_{f,k}\rho_f h_f\right) + \nabla\bullet\left(\alpha_g \rho_g \vec{v}_g h_g + \alpha_e \rho_f \vec{v}_e h_f + \sum_k \alpha_{f,k}\rho_f \vec{v}_{f,k} h_f\right) = \frac{\partial P}{\partial t} + E_{mix,g} + E_{mix,e} + \sum_k E_{fs,k} + \sum_k q_{w,k} \quad (2.1\text{-}8)$$

where subscript k identifies the liquid films in a subchannel.

Several assumptions have been made to derive the governing equations of mass, momentum and energy:

- The momentum transfer terms due vaporization ($\Gamma_g v_r$) and condensation ($\Gamma_l v_r$) have been neglected. This is justifiable as these terms are small compared to the other interfacial forces like the interfacial drag. (For nucleate boiling in a BWR at a power density of 50 kW/ℓ the interfacial force due to mass transfer is $\Gamma_g v_r = \frac{5\bullet 10^7}{h_{fg}} v_r \approx 10$ kg/m^2-sec^2 using $h_{fg} = 1.5\bullet 10^6$ J/kg and $v_r = 0.3$ m/sec, whereas the interfacial drag balancing the buoyancy is given by $\alpha(1\text{-}\alpha)\,\Delta\rho g \approx 1.6\ 10^3$ kg/m^2-sec^2, using $\alpha = 0.4$ and P = 7 MPa).
- Pressures in all fields are assumed to be the same ($P_g = P_{gi} = P_{li} = P_l = P$). In general, this pressure difference is small and the impact on the calculation is negligible. This assumption simplifies the equations since only one pressure needs to be calculated.
- The pressure difference between the phases due to interphase curvature is neglected. This term has little impact on the fluid properties and does not impact the relative motion of the phases. (For particles with a radius of 10^{-4} m the pressure change across the interface is less than 10^3 Pa for typical BWR operating conditions

- The shear tensor is neglected except for shear at the boundaries against solid structures and shear at the interface for seperated flow. The shear against the solid boundaries is accounted for through wall friction terms F_{we}, F_{wg}, and F_{wf}. The shear at the interface is accounted for through drag terms F_{ie} and F_{if} which can be correlated using the relative velocity.
- Conductive heat transfer ($\vec{\nabla} \bullet (k\vec{\nabla}T)$) in the fluid has been neglected except for heat transfer to solid structures, which is included as the wall heat transfer terms q_{wg} and $q_{w\ell}$, and heat transfer at the interface q_{ig} and $q_{i\ell}$. Neglecting conductive energy transfer within the fluid is justified as it is much smaller than the convective heat transfer for steam water mixtures.
- The flow is at sufficiently low speed such that kinetic and potential energy are small compared to internal energy ($\frac{\vec{U}^2}{2} \ll e$ so that $e \approx i$).

2.2 Constitutive Correlations

To close the set of the basic equations described in section 2.1, a set of constitutive correlations describing wall and interfacial shear, wall and interfacial heat transfer, mixing and void drift, entrainment and deposition, and film spreading are needed. These correlations define the rate of exchange of mass, momentum, and energy between the phases and their surrounding. They take on different forms for different flow patterns, and therefore it is important to identify the flow regime in each hydraulic cell before proceeding with solution of flow equations for that cell. This will be the objective of the following section.

2.2.1 Flow Regime Map

Since shear and heat transfer at vapor–liquid interfaces and wall surfaces vary among flow regimes, COBRAG utilizes a flow regime map (Table 2-1) for determining these quantities. The flow regime map utilized in COBRAG is divided into two major flow regimes: (a) the liquid continuous flow regime at low void fraction and (b) the vapor continuous flow regime at high void fraction with a transition zone in between. The liquid continuous flow regime includes single–phase liquid flow and bubbly/churn flow. The vapor continuous flow regime includes dispersed annular droplet flow and single–phase vapor flow. The transition regime involves churn to annular and churn to droplet; depending on the void fraction, flow rate and other variables. During the transition to annular flow, COBRAG splits liquid flow into droplets and film flow such that there is equilibrium between the entrainment rate and droplet rate. The transition criteria can be summarized as follows:

Liquid continuous flow:

$$\alpha_g \leq \alpha_{tran} - 0.1 \tag{2.2.1}$$

Transition flow:

$$\alpha_{tran} - 0.1 < \alpha_g < \alpha_{tran} \tag{2.2.2}$$

Vapor continuous flow:

$$\alpha_g \geq \alpha_{tran} \tag{2.2.3}$$

A transition regime of 0.1 in void fraction has been found to produce good agreement with void fraction data [2]. It also assures a smooth transition in the constitutive correlations and avoids discontinuities, which tend to cause numerical problems. The transition to annular flow is given by:

$$\alpha_{tran} = \left(1+4\frac{\rho_g}{\rho_\ell}\right)\frac{1}{C_o} - 4\frac{\rho_g}{\rho_\ell}$$
$$C_o = C_\infty\left(C_\infty - 1\right)\sqrt{\frac{\rho_g}{\rho_\ell}};\quad C_\infty = 1.393 - 0.015\ \ln(Re) \tag{2.2.4}$$

where Re, is the Reynolds number given by

$$Re = \frac{GD_h}{\mu_l} \tag{2.2.5}$$

The criterion for transition to annular flow is when the liquid in the film (or entrained droplets) can be lifted by the vapor flow [3, 4].

The liquid continuous flow regime is subdivided into two flow regimes. (1) Bubbly flow is assumed for $\alpha_g < 0.3$, and (2) churn flow is assumed for $0.3 < \alpha_g < \alpha_{tran} - 0.1$

Table 2-1. COBRAG Flow Regime Map

Void Fraction	Flow Regime
0.0	Single Phase Liquid
$0.0 < \alpha_g < 0.3$	Bubbly Flow
$0.3 < \alpha_g < \alpha_{tran} - 0.1$	Churn Flow
$\alpha_{tran} - 0.1 < \alpha_g < \alpha_{tran}$	Transition Regime
$\alpha_{tran} < \alpha_g < 1.0$	Dispersed Annular Flow
1.0	Single Phase Vapor

2.2.2 Interfacial Shear

Calculation of interfacial shear and momentum exchange across the interface is a necessary part of the two-fluid equation system solution. In specific terms, the interfacial shear model calculates the variable f_{ie} in the equations of motion for vapor and liquid and f_{if} in the liquid film momentum. Those forces represent the drag force, per unit volume, between the phases $f_{\ell g}$; it is expressed in terms of average phasic velocity difference:

$$f_{\ell g} = c_i |\bar{v}_r| \bar{v}_r \tag{2.2.6}$$

where c_i is the local average interfacial drag coefficient between phases (per unit volume) and $\bar{v}_r$ is the void-weighted average velocity difference between vapor and liquid. The local values of c_i and $\bar{v}_r$ are dependent on flow regime, void fraction and properties of vapor and liquid (c_ii is a function of $\bar{v}_r$). Equation 2.2.6 gives only the generic form of $f_{\ell g}$ (its specific forms are described later). The basic principle of these calculations is to identify the prevailing flow pattern at each hydraulic junction and then apply specific correlations for relative phasic velocity and interfacial drag to determine the momentum exchange across the interface at that junction.

2.2.2.1 Background

The bulk of the data available for the evaluation of the interfacial shear and the wall friction are void fraction and pressure drop data. These are also the parameters that are important and must be described accurately in a best-estimate analysis of the two-phase flow in a BWR. More fundamental data are available for the shear and the interfacial forces, and extensive basic research is continuing. However, a comprehensive set of models for the shear and interfacial forces for all flow regimes does not presently exist, and the models that do exist are primarily for idealized flow regimes. For these reasons, the development of the constitutive correlations for the interfacial shear is based on the very large database that exists for void fractions and pressure drop. The correlations are based on the following:

- For adiabatic and steady state conditions, the two-fluid model and the drift flux model are equivalent, and drift flux parameters can be used to characterize the relative velocity, and the phase and flow distributions.
- The correlations for the interfacial shear and drag, as well as wall friction, as derived from adiabatic steady-state conditions, are applicable for transient conditions.

The interfacial shear correlations are based on the set of drift flux correlations developed by Ishii [3] from void fraction data available in literature.

2.2.2.2 Relation to Drift Flux Parameters

The relation between interfacial forces and drift flux parameters is discussed in detail in Reference [3,7]. A brief summary will be given in the following sections.

2.2.2.2.1 *Shear and Wall Friction*

The presence of wall friction creates a shear field in the two-phase flow. This shear field will interact with both phases, and thus create an interfacial force, which has its origin in the wall friction. For example, for steady-state bubbly flow, the momentum equations can be written as:

$$0 = -\alpha \frac{\partial P}{\partial x} - \alpha \rho_g g - f_{\ell g} \qquad \text{[for the vapor phase]} \tag{2.2.7}$$

$$0 = -(1-\alpha) \frac{\partial P}{\partial x} - (1-\alpha) \rho_\ell g + f_{\ell g} - F_w \qquad \text{[for the liquid phase]} \tag{2.2.8}$$

where $f_{\ell g}$ represents the shear at the interface, and F_w represents the shear between the wall and the liquid. If the pressure gradient is eliminated from the above equations, one obtains:

$$f_{\ell v} = \Delta\rho g\alpha(1-\alpha) + \alpha F_w \tag{2.2.9}$$

Consequently, if the interfacial shear above was a function only of the relative velocity between the phases, the relative velocity would be dependent upon the wall friction or the Reynolds number. This, however, is not the case. Data [3,10] indicate that the drift velocity is virtually independent of the flow rate. The interfacial shear, therefore, consists of another term with its origin in the wall friction besides a term that is a function of the relative velocity.

Following Ishii's [3] notation , the local time-averaged momentum equations for the vapor and liquid phases are:

$$\alpha\rho_g\left(\frac{\partial \bar{v}_g}{\partial t} + \bar{v}_g \bullet \nabla \bar{v}_g\right) = -\alpha\nabla P + \alpha\nabla \bullet \bar{\bar{\tau}} - \alpha\rho_v \bar{g} - \bar{M}_g \tag{2.2.10}$$

$$(1-\alpha)\rho_\ell\left(\frac{\partial \bar{v}_\ell}{\partial t} + \bar{v}_\ell \bullet \nabla \bar{v}_\ell\right) = -(1-\alpha)\nabla P + (1-\alpha)\nabla \bullet \bar{\bar{\tau}} - (1-\alpha)\rho_\ell \bar{g} + \bar{M}_g \tag{2.2.11}$$

Here the interfacial mass transfer has been neglected and it has been assumed that each phase, as well as the interface, has the same pressure.

For one-dimensional flow, Equations (2.2.10) and (2.2.11) degenerate to:

$$\alpha\rho_g\left(\frac{\partial v_g}{\partial t} + v_g \cdot \nabla v_g\right) = -\alpha\frac{\partial P}{\partial z} + \alpha\nabla \cdot \bar{\tau}_z - \alpha\rho_g g - M_g \tag{2.2.12}$$

$$(1-\alpha)\rho_\ell\left(\frac{\partial v_\ell}{\partial t} + v_\ell \bullet \nabla v_\ell\right) = -(1-\alpha)\frac{\partial P}{\partial z} + (1-\alpha)\nabla \bullet \bar{\tau}_z - (1-\alpha)\rho_\ell g + M_g \tag{2.2.13}$$

An interpretation of the various terms on the right-hand side of equation (2.2.12) and (2.2.13) can be obtained from Figure 2-1

For the gas equation, the interpretation of the various terms is as follows:

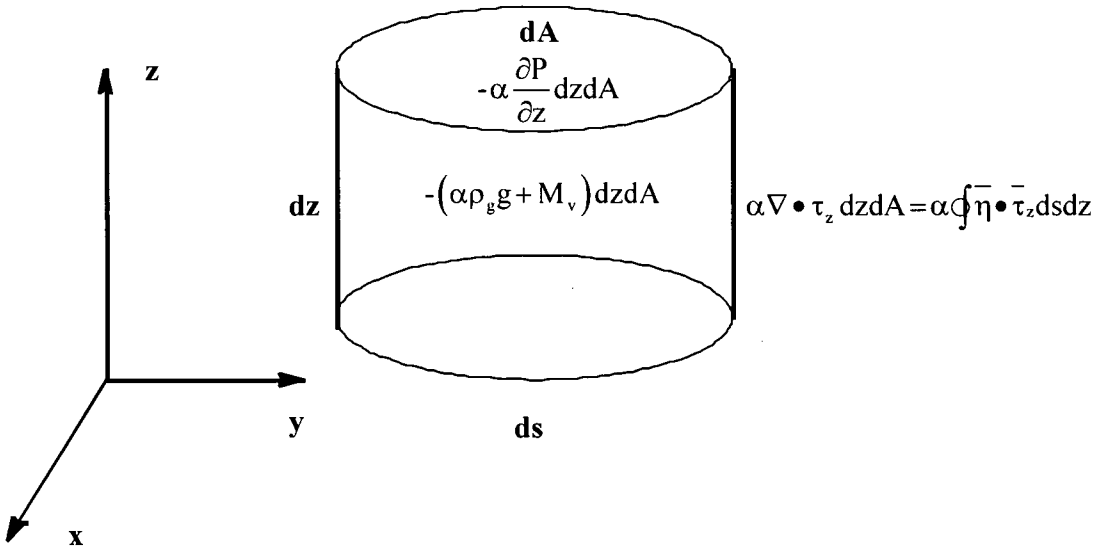

Figure 2-1. Right-Hand Side of Vapor Momentum Equation

$-\alpha\frac{\partial P}{\partial z}$ = the force on the gas due to the pressure gradient in the z-direction (the pressure is assumed to be the same for each phase)

$\alpha\nabla\cdot\bar{\tau}_z$ = the force on the gas due to the shear at the surface of the incremental volume. It is assumed that the averaged shear tension is the same for each phase, which is reasonable, because, except for surface tension and mass transfer effects, the shear is a continuous function.

$-\alpha\rho_v g$ = the body force, due to gravity, on the gas.

M_g = the interfacial drag between the phases inside the incremental volume due to a local difference in the phase velocities.

The bases for the interfacial shear model are stated in Section 2.2.2.1 For adiabatic and steady state conditions in a straight fluid channel without any area changes, there is no acceleration of the fluid and the $\frac{\partial}{\partial t}$ as well as the $\frac{\partial}{\partial x}$ terms are zero. Therefore, for adiabatic steady-state conditions, Equations (2.2.12) and (2.2.13) reduce to:

$$\alpha\frac{\partial P}{\partial z}-\alpha\nabla\bullet\bar{\tau}_z+\alpha\rho_g g+M_g=0 \tag{2.2.14}$$

$$(1-\alpha)\frac{\partial P}{\partial z}-(1-\alpha)\nabla\bullet\bar{\tau}_z+(1-\alpha)\rho_\ell g-M_g=0 \tag{2.2.15}$$

When Equations (2.2.14) and (2.2.15) are added,

$$\frac{\partial P}{\partial z}-\nabla\bullet\bar{\tau}_z+\left((1-\alpha)\rho_\ell+\alpha\rho_g\right)g=0 \tag{2.2.16}$$

The integration of this equation over the cross section, assuming that the densities and the pressure gradient are constant across the flow area, results in:

$$A\frac{\partial P}{\partial z}-\int_S\bar{\eta}\bullet\bar{\tau}_z ds+A\left(\langle 1-\alpha\rangle\rho_\ell+\langle\alpha\rangle\rho_g\right)g=0 \tag{2.2.17}$$

The integral is along the boundary (S), $\bar{\eta}$ is the normal to the boundary, and Gauss's theorem has been used. When Equations (2.2.16) and (2.2.17) are combined,

$$\nabla\cdot\bar{\tau}_z=\frac{1}{A}\int\bar{\eta}\bullet\bar{\tau}_z ds-\Delta\rho g\left(\alpha-\langle\alpha\rangle\right) \tag{2.2.18}$$

Integrating the momentum equation for the gas over the cross section results in:

$$\langle\alpha\rangle A\frac{\partial P}{\partial z}-\int_A\alpha\nabla\bullet\bar{\tau}_z dA+\langle\alpha\rangle A\rho_g g+\int_A M_g dA=0 \tag{2.2.19}$$

The second term in this equation can be evaluated using Equation (2.2.18)

$$\int_A\alpha\nabla\bullet\bar{\tau}_z dA=\langle\alpha\rangle\int\bar{\eta}\bullet\bar{\tau}_z ds-A\Delta\rho g\left\langle\left(\alpha-\langle\alpha\rangle\right)^2\right\rangle \tag{2.2.20}$$

The left side of Equation (2.2.20) is the total amount of shear on the vapor phase. The first term on the right side is the void fraction times the wall friction. The second term is an induced shear stress due to the variance of the void fraction across the flow area:

$$f_i=A\Delta\rho g\left\langle\left(\alpha-\langle\alpha\rangle\right)^2\right\rangle \tag{2.2.21}$$

and from which

$$\int_A\alpha\nabla\bullet\bar{\tau}_z dA=-\langle\alpha\rangle F_w-f_i \tag{2.2.22}$$

Inserting this into Equation (2.2.19) gives:

$$\langle\alpha\rangle A\frac{\partial P}{\partial z}+\langle\alpha\rangle F_w+f_i+\langle\alpha\rangle A\rho_g g+\int_A M_g dA=0 \tag{2.2.23}$$

Similarly, for the liquid momentum equation,

$$\langle 1-\alpha\rangle A\frac{\partial P}{\partial z}+\langle 1-\alpha\rangle F_w-f_i+\langle 1-\alpha\rangle A\rho_f g-\int_A M_g dA=0 \tag{2.2.24}$$

The various terms in the integrated momentum equation for the gas have the following physical interpretations:

$\langle\alpha\rangle A\frac{\partial P}{\partial z}$ = the force due to the pressure gradient

$\langle\alpha\rangle F_w$ = induced shear stress due to the shear created by the wall friction

$\langle\alpha\rangle A\rho_g g$ = the body force due to gravity

$\int_A M_g dA$ = the drag force between the phases due to local velocity differences

f_i = induced shear stress due to the radial phase distribution

The terms in the integrated liquid momentum equation can, of course, be interpreted in the same way.

Consequently, if the liquid phase alone is in contact with the wall, the wall friction acts alone on the liquid, giving:

$$F_{wg}=0 \tag{2.2.25}$$

$$F_{wf}=F_w \tag{2.2.26}$$

The induced shear, however, caused by the wall friction, creates an interfacial force between the phases given by $\langle\alpha\rangle F_w$ where the net forces on the phases due to the wall friction become $\langle\alpha\rangle F_w$ for the gas phase and $\langle 1-\alpha\rangle F_w$ for the liquid phase. Similarly, if the gas phase is in contact with the wall,

$$F_{wg}=F_w \tag{2.2.27}$$

$$F_{wf}=0 \tag{2.2.28}$$

It is significant to realize that the distribution of the wall shear between the phases has no impact on the pressure drop, as the total momentum equation is not affected. The distribution, however, affects the interaction between the phases and is in agreement with the experimental observation [3, 10] that the relative velocity is insensitive to flow rate.

2.2.2.2.2 *Interfacial Drag and Phase Distribution*

In Section 2.2.2.2.1 the interfacial force due to the wall friction was derived. The remaining interfacial forces then become a function of the interfacial drag due to the difference in the phase velocities, the buoyancy due to the gravity, and a force that is due to the phase distribution.

When $\frac{\partial P}{\partial z}$ and τ are eliminated from Equations (2.2.14) and (2.2.15)

$$M_g = \alpha(1-\alpha)\Delta\rho g \tag{2.2.29}$$

The physical interpretation of this equation is that, locally, the drag is equal to the buoyancy. Integrating this equation over the cross section gives:

$$\int_A M_g dA = A\Delta\rho g\langle\alpha(1-\alpha)\rangle \tag{2.2.30}$$

This equation, combined with Equation (2.2.21), gives the total interaction between the phases due to drag or shear:

$$\langle f_{\ell g}\rangle = f_i + \int_A M_g dA = A\Delta\rho\langle\alpha\rangle\langle 1-\alpha\rangle \tag{2.2.31}$$

For Fully dispersed flow,

$$f_i = 0 \text{ and } \langle f_{\ell g}\rangle = \int_A M_g dA = A\Delta\rho g\langle\alpha(1-\alpha)\rangle \tag{2.2.32}$$

This implies that the interaction between the phases is solely due to the drag between the phases. There is no shear between the phases, except for the term due to the wall friction.

Similarly for fully separated flow, e.g., annular flow,

$$\langle f_{\ell g}\rangle = f_i = A\Delta\rho g\langle\alpha(1-\alpha)\rangle \text{ and } \int_A M_g dA = 0 \tag{2.2.33}$$

The interaction is given by the shear at the interface. There is no local drag.

In either case or any combination, however, the total interaction between phases, except for the force due to the wall shear is given by equation (2.2.31).

The interfacial force must be related to the velocity difference between the phases. It is conventional to define:

$$f_{\ell g} = c_i |v_r| v_r \tag{2.2.34}$$

Integrating Equation (2.2.34) over the cross section yields:

$$A\langle f_{\ell g}\rangle = \int_A f_{\ell g} dA = A\bar{c}_i |\bar{v}_r| \bar{v}_r \tag{2.2.35}$$

where:

$$\bar{c}_i = \frac{\langle c_i |v_r| v_r\rangle}{|\langle v_r\rangle| \langle v_r\rangle} \tag{2.2.36}$$

In this equation, $\bar{v}_r$ is a weighted average value for the relative velocity. It is important to note that $\bar{v}_r \neq \bar{v}_g - \bar{v}_\ell$, since $\bar{v}_g = \langle \alpha v_g\rangle / \langle \alpha\rangle$ and $\bar{v}_\ell = \langle (1-\alpha) v_\ell\rangle / \langle 1-\alpha\rangle$ have different weight functions. We will only have $\bar{v}_r = \bar{v}_g - \bar{v}_\ell$ for a uniform phase or velocity distribution.

Locally, the drift flux velocity is related to the relative velocity by:

$$v_r = \frac{v_{gj}}{(1-\alpha)} \tag{2.2.37}$$

and, consequently, an average relative velocity can be defined by:

$$\bar{v}_r = \frac{\bar{v}_{gj}}{\langle 1-\alpha\rangle} \tag{2.2.38}$$

where

$$\bar{v}_{gj} = \langle \alpha v_{gj}\rangle / \langle \alpha\rangle \tag{2.2.39}$$

Eliminating $\bar{v}_{gj}$ using the drift flux correlation:

$$\bar{v}_g = C_o \langle j\rangle + \bar{v}_{gj} \tag{2.2.40}$$

where

$$C_o = \langle \alpha j\rangle / (\langle \alpha\rangle \langle j\rangle) \tag{2.2.41}$$

yields

$$\bar{v}_r = \frac{1 - \langle \alpha\rangle C_o}{\langle 1-\alpha\rangle} \bar{v}_g - C_o \bar{v}_\ell \tag{2.2.42}$$

This expression, combined with Equation (2.2.35), results in:

$$\langle f_{fg} \rangle = \bar{c}_i \left| \frac{1-\langle\alpha\rangle C_o}{\langle 1-\alpha \rangle} \bar{v}_g - C_o \bar{v}_f \right| \left(\frac{1-\langle\alpha\rangle C_o}{\langle 1-\alpha \rangle} \bar{v}_g - C_o \bar{v}_f \right) \tag{2.2.43}$$

Thus, using Equation (2.2.31) and with Co and $\bar{v}_{gj}$ correlated from void fraction data, the interfacial interaction can be evaluated by:

$$\bar{c}_i \left| \frac{1-\langle\alpha\rangle C_o}{\langle 1-\alpha \rangle} \bar{v}_g - C_o \bar{v}_f \right| \left(\frac{1-\langle\alpha\rangle C_o}{\langle 1-\alpha \rangle} \bar{v}_g - C_o \bar{v}_f \right) = \Delta\rho g \langle\alpha\rangle \langle 1-\alpha \rangle \tag{2.2.44}$$

or in another form

$$\bar{c}_i \left| C_1 \bar{v}_g - C_o \bar{v}_f \right| \left(C_1 \bar{v}_g - C_o \bar{v}_f \right) = \Delta\rho g \langle\alpha\rangle \langle 1-\alpha \rangle \tag{2.2.45}$$

where:

$$C_1 = \frac{1-\langle\alpha\rangle C_o}{\langle 1-\alpha \rangle} \tag{2.2.46}$$

Using equation (2.2.38), equation (2.2.44) can be written as

$$\bar{c}_i \frac{\left| \bar{v}_{gj} \right| \bar{v}_{gj}}{\langle 1-\alpha \rangle^2} = \Delta\rho g \langle\alpha\rangle \langle 1-\alpha \rangle \tag{2.2.47}$$

where:

$$\bar{v}_{gj} = (1-\langle\alpha\rangle C_0) \bar{v}_{gj} - \langle 1-\alpha \rangle C_0 \bar{v}_f \tag{2.2.48}$$

For fully dispersed flow, the local drag can be given by a drag coefficient in the form of

$$M_g = \frac{1}{8} \frac{C_D}{d_i} \rho_c \left| v_r \right| v_r \tag{2.2.49}$$

where ρ_c is the density of the continuous phase, and $\frac{1}{d_i}$ is the interfacial area per unit volume.

Combining equations, (2.2.38) and (2.2.49) gives

$$\langle f_{fg} \rangle = \frac{1}{8} \frac{\bar{C}_D}{d_i} \rho_c \frac{\left| \bar{v}_{gj} \right| \bar{v}_{gj}}{\langle 1-\alpha \rangle^2} = \Delta\rho g \langle\alpha\rangle \langle 1-\alpha \rangle \tag{2.2.50}$$

Equation (2.2.50) is used to develop correlations for the interfacial shear for bubbly and churn flow.

2.2.2.3 · Bubbly/Churn Flow

For bubbly flow, the interfacial stress is calculated according to equation (2.2.45) as:

$$f_i = \frac{1}{8}\frac{C_D}{d_i}\rho_c |C_1 v_g - C_o v_\ell| (C_1 v_g - C_o v_\ell) \tag{2.2.51}$$

with

$$\bar{c}_i = \frac{1}{8}\frac{C_D}{d_i}\rho_c \tag{2.2.52}$$

Furthermore, the liquid is the continuous phase, so that:

$$\rho_c = \rho_\ell \tag{2.2.53}$$

and the interfacial area per unit volume can be given in terms of a critical Weber number:

$$\frac{1}{d_i} = 6\langle\alpha_g\rangle \frac{\rho_\ell \bar{v}_{gj}^{\,2}}{\sigma We_c \langle 1-\alpha_g\rangle^2} \tag{2.2.54}$$

Combining Equations (2.2.53), (2.2.54) and (2.2.50) gives:

$$\frac{3}{4}\langle\alpha_g\rangle \frac{C_D}{We_c}\frac{\rho_\ell^{\,2}}{\sigma}\frac{\bar{v}_{gj}^{\,4}}{\langle 1-\alpha_g\rangle^4} = \Delta\rho g \langle\alpha_g\rangle\langle 1-\alpha_g\rangle \tag{2.2.55}$$

Many expressions for $\bar{v}_{gj}$ for co–current flow have been reported in the literature [8, 9], and most are of the form:

$$\bar{v}_{gj} = k\left\{\frac{\Delta\rho g\sigma}{\rho_\ell^2}\right\}^{0.25} \tag{2.2.56}$$

where k ranges from 1.18 to 1.53. A value for k of 1.53 fits a wide range of data. Inserting equation (2.2.56) into Equation (2.2.55) results in:

$$\frac{C_D}{We_c} = 0.2433\langle 1-\alpha_g\rangle^5 \tag{2.2.57}$$

In order to specify the interfacial shear, the exact value of We_c is not needed, only the ratio C_D/ We_c matters. For the interfacial heat transfer, however, d_i and We_c are important, and $We_c = 6.5$ is used to specify the average particle size.

For co–current flow, the distribution parameter will range from 0 for subcooled boiling to 1.333 as a maximum value for parabolic profiles. For high flow rates or high pressure ($\rho_g \approx \rho_l$), the distribution parameter should approach 1. Ishii [3] recommends at low void fraction:

$$C_{o,l}=C_\infty-(C_\infty-1)\sqrt{\frac{\rho_g}{\rho_\ell}} \tag{2.2.58}$$

where C_∞ is given by Nikuradse [11]:

$$C_\infty = 1.393 - 0.015 \ln(Re) \tag{2.2.59}$$

where

$$Re=\frac{GD_h}{\mu_\ell} \tag{2.2.60}$$

Since the distribution parameter should be continuous at the transition to annular flow, to avoid discontinuity in void fraction, and since C_o must approaches 1 as the void fraction approaches unity, Ishii's expression (equation (2.2.58) is modified in COBRAG using parabolic relation to directly satisfy these constrains:

[[ ]] (2.2.61)

where

[[ ]] (2.2.62)

For subcooled boiling, the vapor is concentrated at the wall, where the liquid velocity approaches zero. Consequently, for subcooled boiling, the distribution parameter should also approach zero, and become zero at the point of net vapor generation. A modification to C_o for subcooled boiling that has the right limits was suggested by Findlay Dix [5]:

[[ ]] (2.2.63)

where $h_{\ell d}$ is the liquid enthalpy at the point of net vapor generation and is given by:

$$h_{\ell d} = \begin{cases} h_f - 154\dfrac{q''_w}{\rho_\ell v_\ell} & \text{if } Pe > 70000 \\ h_f - 0.0022\dfrac{q''_w D_h C_{p,\ell}}{k_\ell} & \text{if } Pe < 70000 \end{cases} \quad (2.2.64)$$

where Pe is the Peclet number defined as:

$$Pe = \frac{G_\ell D_h C_{p,\ell}}{k_\ell} \quad (2.2.65)$$

and q''_w is the wall heat flux, which goes to heat up the liquid.

2.2.2.4 Annular flow

For annular flow the interfacial shear is calculated by [12]:

$$f_f = \frac{2}{D_h}\rho_g c_f |v_g - v_f|(v_g - v_f) \quad (2.2.66)$$

The volume fraction α_f, which occupied by liquid film, is:

$$\alpha_f = 1 - \alpha \quad (2.2.67)$$

the interfacial friction coefficient is given according to Wallis [12] as:

$$c_f = 0.005\frac{1 + 75\alpha_f}{(1 - \alpha_f)^{5/2}} \quad (2.2.68)$$

Since annular flow involves high void fraction, α_f is small, and thus:

$$(1 - \alpha_f)^{5/2} \approx (1 - .5\alpha_f)^5 \quad (2.2.69)$$

Inserting equation (2.2.69) into (2.2.68), one obtains:

$$c_f = 0.005\frac{1 + 75\alpha_f}{(1 - .5\alpha_f)^5} \quad (2.2.70)$$

2.2.2.5 Droplet Flow

For droplet flow, the interfacial shear is calculated similarly to bubbly flow [3]:

$$f_{eg} = \frac{1}{8}\frac{C_D}{d_i}\rho_c |C_1 v_g - C_o v_e|(C_1 v_g - C_o v_e) \tag{2.2.71}$$

Furthermore, the continuous phase is the vapor phase:

$$\rho_c = \rho_g \tag{2.2.72}$$

The volume fraction α_e occupied by a droplet is:

$$\alpha_e = 1 - \alpha_c \tag{2.2.73}$$

The interfacial area in the droplet flow regime depends on the number of droplets and average droplet diameter:

$$A_{ie} = N_e \pi d_e^2 \tag{2.2.74}$$

The number of droplets N_d is related to the droplet fraction:

$$N_e = \frac{6\alpha_e}{\pi d_e^3} \tag{2.2.75}$$

Substituting Equation (2.2.75) into Equation (2.2.74), one obtains the expression for the interfacial flow area per unit volume:

$$\frac{1}{d_i} = \frac{6\alpha_e}{d_e} \tag{2.2.76}$$

Droplet diameter is calculated from the critical Weber number. For low flow rates, the initial relative velocity for the droplet, as it is entrained from the film is used:

$$d_e = \frac{W_{ec}\sigma}{\rho_g v_{re}^2} \tag{2.2.77}$$

where v_{re} is the relative velocity given by:

$$v_{re} = v_g - v_f = \frac{\overline{v}_{gj}}{<1-\alpha>} \tag{2.2.78}$$

combining equations (2.2.76), (2.2.77), (2.2.78), (2.2.50), gives

$$f_{eg} = \frac{3}{4}\frac{\alpha_e}{\sigma}\frac{C_D}{We_c}\rho_g^2\frac{v_{gj}^4}{<1-\alpha>^4} = \Delta\rho g\langle\alpha\rangle\langle 1-\alpha\rangle \tag{2.2.79}$$

Many expressions for $\bar{v}_{gj}$ are reported in the literature [12] and most are of the form:

$$\bar{v}_{gj} = k\,(1-\alpha)\left\{\frac{\Delta\rho g\sigma}{\rho_g^{\,2}}\right\}^{0.25} \tag{2.2.80}$$

Ishii [3], recommends k = 1.41.

Using Equation (2.2.80) and $k = 1.41 = \sqrt{2}$, Equation (2.2.79) gives:

$$\frac{C_D}{We_c} = \frac{1}{3}<\alpha> \tag{2.2.81}$$

the average core void fraction $<\alpha>$ is given by:

$$\alpha_g^+ = \frac{\alpha_g}{\alpha_e + \alpha_g} \tag{2.2.82}$$

equation (2.2.82) indicates that in order to specify the interfacial shear, the exact value of We_c is not needed ; only the ratio of $\frac{C_D}{We_c}$ matters.

combining equations (2.2.82), (2.2.81), and (2.2.79), gives:

$$f_e = \frac{1}{4\sigma}\alpha_e\alpha_g^+\rho_g^2 v_{Re}^4 \tag{2.2.83}$$

where the average relative velocity between the droplets and the vapor is given by:

$$v_{Re} = \frac{1-\alpha_g^+ C_o}{1-\alpha_g^+}v_g - C_o v_e \tag{2.2.84}$$

C_o in equation (2.2.84) is given by Equation (2.2.61).

For large flow rates where the droplets are created by entrainment from the film, the droplet size will be determined by the initial relative velocity as they are entrained from the film on the wall. Since the film velocity is much smaller than the vapor velocity and the void fraction is high, the initial relative velocity can be approximated by the total flux. Thus, assuming a critical Weber number of 12, this is in agreement with Ishii's recommendations and leads to:

$$\frac{1}{d_i}=\frac{1}{2}(1-\alpha)\frac{\rho_g j^2}{\sigma} \tag{2.2.85}$$

The droplets produced by the entrainment process can mainly be characterized as undistorted particles outside the Stokes regime, and an approximation [3] for the drag coefficient is:

$$C_D = 1.07\,\alpha\,Re_e^{-0.5} \tag{2.2.86}$$

where:

$$Re_e = \frac{\rho_g\, d_e\, v_{re}}{\mu_g} \tag{2.2.87}$$

the droplet diameter is calculated from the critical Weber number of 12:

$$d_e = \frac{12\sigma}{\rho_g v_{re}^2} \tag{2.2.88}$$

Combining equations (2.2.87), (2.2.88), (2.2.86), (2.2.85) and (2.2.79), one obtains:

$$f_e = .8025\alpha_e\alpha_g^{+}\sqrt{\frac{\rho_g\mu_g}{d_e^3}}v_{Re}^{1.5} \tag{2.2.89}$$

Equating equation 2.2.81 to 2.2.89, and solve for the transition droplet diamter d_t, one can obtain the range of applicability of each equation and the transition from one to another:

$$f_e=\begin{cases}\dfrac{1}{4\sigma}\alpha_e\alpha_g'\rho_g^2 v_{Re}^4 & \text{for } d_e \geq d_t \\ 0.8025\alpha_e\alpha_g'\sqrt{\dfrac{\rho_g\mu_g}{d_d^3}}v_{Re}^{1.5} & \text{for } d_e < d_t\end{cases} \tag{2.2.90}$$

where the transition droplet diameter is given by

$$d_t = \frac{2.176}{\rho_g}\left(\frac{\sigma^2\mu_g}{v_{Re}^5}\right)^{1/3} \tag{2.2.91}$$

2.2.3 Wall friction and singular losses

The wall friction in COBRAG incorporates both wall shear and singular or form losses. The wall shear is calculated using a two-phase multiplier approach as:

$$F_W = \frac{1}{2}\frac{f_\ell}{D}\frac{G^2}{\rho_\ell}\varphi_{\ell o}^2 \tag{2.2.92}$$

where $\varphi_{\ell o}^2$ is the two-phase multiplier, and f_ℓ is the single friction factor.

The single-phase friction factor is calculated from fit to the Moody curves given Waggener [37]:

$$f_k = \begin{cases} \dfrac{64}{Re_k} & \text{for } Re < 1084 \\ 0.0055\left[1+\left(2\times10^4\dfrac{\varepsilon}{D_h}+\dfrac{10^6}{Re_k}\right)^{1/3}\right] & \text{for } Re > 1084 \end{cases} \tag{2.2.93}$$

where:

$$Re_k = \frac{GD_h}{\mu_k} \tag{2.2.94}$$

and k can be liquid ℓ or vapor g.

COBRAG employs a two-phase multiplier, $\Phi_{\ell o}^2$, which is of the Martinelli-Nelson Type. The two –phase frictional multiplier used COBRAG is based on a modification to the Chisholm correlation. Following a traditional separated flow approach, Chisholm proposed a correlation of the form:

$$\frac{\Delta P_{TP}}{\Delta P_{\ell o}} = \Phi_{\ell o}^2 = (1-x)^2\left(1+\frac{C}{X}+\frac{1}{X^2}\right) \tag{2.2.95}$$

where X is the Lockhart-Martinelli parameter given by:

$$1/X^2 = \frac{f_g x^2}{\rho_g}\Big/\frac{f_\ell (1-x)^2}{\rho_\ell} = \varsigma\frac{x^2}{(1-x)^2} \tag{2.2.96}$$

where:

$$\zeta = \frac{\rho_\ell f_g}{\rho_g f_\ell} \tag{2.2.97}$$

and the two–phase multiplier is given by:

[[ ]](2.2.98)

The modification to the Chisholm correlation are based on extensive comparisons to rod bundle pressure drop data [5, 6] from BWR bundles with 7x7 and 8x8 lattices.

For the liquid continuous flow regime, the wall friction is distributed between the phases proportional to the void fraction [7], and for the dispersed annular flow regime the entire wall friction is applied to the liquid.

The pressure drop due to singular losses in the spacer elements is calculated separately for the film and the core flow. For the liquid continuous flow regime, where no film exists, the core flow is equal to the total flow, and for the dispersed annular flow regime the core flow is the vapor and droplet flow.

2.2.3.1 Two-Phase Flow Pressure Drop

The flow through an abrupt area change can be visualized by considering each phase to be flowing in a phasic stream tube. The velocities and volume fractions are calculated from the transient flow equations in the upstream and downstream regions. Within the area change region, the phases are coupled through the inter-phase drag and a common pressure gradient. The gradient in relative velocity can be large at points of abrupt area changes. Since each phase is governed by a modified Bernoulli type of equation, it is reasonable to assume that losses associated with changes in phasic flow area can be modeled by separate dynamic pressure loss terms for both the liquid and gas phases. However, the interfacial drag effects are important at abrupt area changes. These will affect the local slip between the phases and the effective phasic areas. In practice, the assumption of flow homogenization at the area change location yields reasonable results. With this assumption, the pressure drop due to singular losses is calculated in COBRAG using the homogeneous two-phase multiplier [6-2]:

$$\Delta P_c = \frac{1}{2} 1.25 \varphi_c^2 |G_c| G_c \qquad (2.2.99)$$

where:

[[

(2.2.100)

(2.2.101)

(2.2.102)

(2.2.103)

(2.2.104)

(2.2.105)

(2.2.106)

]](2.2.107)

and

$$\varphi^2_{\ell o,\text{hom}} = 1 + x_c \frac{\nu_{\ell g}}{\nu_\ell} \quad (2.2.108)$$

x_c in equation (2.2.100) denotes the vapor flow quality of the core flow for vapor continuous flow regimes, and vapor flow quality for the entire flow for the liquid continuous flow regimes and α_c^- and α_c^+ designate upstream and downstream void fraction.

The singular loss on the core is distributed between the phases proportional to the void fraction. For the film the singular pressure drop is calculated by:

$$\Delta P_f = \frac{1}{2}\varphi_{cf}{}^2 \rho_\ell |v_f| v_f \tag{2.2.109}$$

where:

[[ ]](2.2.110)

The singular loss on the film is applied entirely to the film.

2.2.4 Wall heat transfer

The steady state model is applied to the wall heat transfer. The total heat transfer at the surface of a structure is equal to its heat generation rate. Since COBRAG is a steady state subchannel analysis code, this model should be adequate.

2.2.5 Interfacial heat transfer

The interfacial heat transfer depends on the interfacial heat transfer coefficient as well as the interfacial area, and a determination of both parameters is important for the total interfacial heat transfer.

2.2.5.1 Background

The COBRAG interfacial heat transfer model is based on the assumption that the liquid-vapor interface is always at saturation temperature corresponding to the local partial steam pressure. Energy exchange rate at the interface provides the necessary mass exchange to maintain the interface at saturation temperature. The total heat exchange and mass transfer at the interface are functions of the volume-averaged liquid-interface heat transfer rate $q_{\ell i}$ and vapor-interface heat transfer rate q_{vi}:

$$q_{\ell i} = A_i h_{i\ell} \left(T_\ell - T_{sat} \right) \tag{2.2.111}$$

$$q_{gi} = A_i h_{ig} \left(T_g - T_{sat} \right) \tag{2.2.112}$$

where A_i is the interfacial area per unit volume and $h_{i\ell}$ and h_{ig} are liquid-interface and vapor-interface convective heat transfer coefficients. Energy exchange at the vapor-liquid interface leads to mass exchange at the interface Γ_g due to evaporation ($\Gamma_g > 0$) or condensation ($\Gamma_g < 0$) processes at the interface:

$$\Gamma_g = \frac{q_{\ell i} + q_{gi}}{h_{fg}} \tag{2.2.113}$$

Equations (2.2.111), (2.2.112) and (2.2.113) represent the energy and mass exchange between phases at the interface and appear in the mass and energy conservation equations. According to Equations (2.2.111) and (2.2.112), interfacial area Ai and interfacial heat transfer coefficients $h_{i\ell}$ and h_{ig} have to be defined (based on the flow regime) to calculate energy and mass exchange at the interface and to close the thermal-hydraulic system of equations. This will be the objective of the following section.

2.2.5.2 Interfacial Area

In the calculation of the interfacial shear, only the ratio between the drag coefficient (CD) and the critical Weber number (We_c) has to be correlated. The interfacial area cannot be obtained explicitly unless the value of the critical Weber number is specified. A maximum stable particle size is given by a critical Weber number of 12–13 [12], and a value of 6.5 is suggested to represent the average particle size. The interfacial area is calculated dependent on the flow regime.

2.2.5.2.1 *Bubbly/Churn Flow*

For bubbly or churn flow, the interfacial area per unit volume is given by:

$$A_{ib} = \frac{1}{d_{ib}} = 6\frac{\alpha_g}{d_b} \tag{2.2.114}$$

where the bubble diameter is calculated from:

$$d_b = \frac{\sigma We_c}{\rho_\ell v_{rb}^2} \tag{2.2.115}$$

the relative phasic velocity is calculated similar to section 2.2.2:

$$v_{rb} = \frac{1-\alpha_g C_o}{1-\alpha_g} v_g - C_o v_\ell = \frac{\overline{v}_{gj}}{(1-\alpha_g)} \tag{2.2.116}$$

the same correlation for the cross-sectional average vapor drift velocity in the interfacial heat transfer and interfacial shear models (see sub-section 2.2.2.3)

$$\overline{v}_{gj} = k\left\{\frac{\Delta\rho g\sigma}{\rho_\ell^2}\right\}^{0.25} \tag{2.2.117}$$

where

k=1.53

2.2.5.2.2 *Droplet Flow*

For droplet flow the interfacial area per unit volume is given by:

$$A_{i,e} = \frac{1}{d_{i,e}} = 6\frac{\alpha_d}{d_e} \tag{2.2.118}$$

where the droplet diameter is defined by:

[[ ]] (2.2.119)

For steady-state applications without boiling transition, thermal equilibrium will exist in the core of the flow, and thus the sensitivity to the vapor from droplet interfacial heat transfer is negligible.

2.2.5.2.3 *Annular Flow*

In this flow regime, interfacial heat transfer and mass exchange occur at the surface of the liquid film on the walls. The interfacial area per unit volume in the annular film flow regime is a function of the average film thickness δ. The volume fraction α_f, which is occupied by liquid film, is:

$$\alpha_f = 1-\alpha \tag{2.2.120}$$

The average film thickness δ and vapor-film interfacial area $A_{i,f}$ per unit volume are given by the film fraction α_f and hydraulic diameter D_h. Assuming a tubular cross section, one obtains:

$$\delta = \frac{D_h}{2}\left(1-\sqrt{\alpha}\right) \tag{2.2.121}$$

$$A_{if} = \frac{4}{D_h}\sqrt{\alpha} \tag{2.2.122}$$

Equation (2.2.122) predicts a non-zero interfacial area

$$A_i = \frac{4}{D_h} \tag{2.2.123}$$

Equation (2.2.121) predicts a film thickness approaching zero as the void fraction approaches one. In reality, at some point the film will break up and not cover the entire surface. COBRAG uses a model for the minimum stable film thickness to model this breakup. The average film thickness δ is limited by the minimum film thickness δ_{min}:

$$\delta = \max\{\delta, \delta_{min}\} \tag{2.2.124}$$

The expression for δ_{min} is derived from the theory of minimum stable film flow and defined as:

$$\delta_{min} = \min \left\{ \left[\frac{18\sigma\mu_\ell^2}{g^2\rho_\ell^3} \right]^{0.2}, \left[\frac{6\sigma\mu_\ell^2}{\rho_\ell\tau^2} \right]^{1/3} \right\} \quad (2.2.125)$$

where the interfacial shear stress is approximated by:

$$\tau = 0.005 \frac{\rho_g v_g^2}{2} \quad (2.2.126)$$

The corresponding value for α_f is:

$$\alpha_{f,min} = \frac{\delta_{min} W_{p,L} \Delta z}{V} \quad (2.2.127)$$

where :

$W_{p,L}$ is the wetted perimiter of surface L adjacent to gap k

Δz and V is the height and volume of the finite difference cell

The film thickness δ will decrease as α_f decreases but remains constant after it reaches the minimum thickness δ_{min}. When $\alpha_f < \alpha_{f,min}$, the vapor-film interfacial area is defined as:

[[(2.2.128)

]](2.2.129)

2.2.5.3 Interfacial Heat Transfer Coefficient

2.2.5.3.1 *Bubbly/Churn flow*

For the bubbly/churn flow regime, the interfacial heat transfer coefficient $h_{i\ell,b}$ for the liquid side is given as follows:

$$h_{i\ell,b} = \frac{k_\ell}{d_b} Nu_{\ell,b} \tag{2.2.130}$$

where the Nusselt number is given by [13]:

$$Nu_{\ell,b} = 2.0 + 0.74\sqrt{\frac{\rho_\ell d_b v_{rb}}{\mu_\ell}} \tag{2.2.131}$$

For the vapor side it is given by [14]:

$$h_{ig,b} = \pi^2 \frac{k_g}{d_b}\left\{2.7\frac{\mu_\ell}{\mu_g}\right\} \tag{2.2.132}$$

The heat transfer coefficient on the vapor side has been increased by a factor of $2.7(\mu_\ell/\mu_g)$ to include the effect of internal circulation in the bubble.

2.2.5.3.2 *Droplet Flow*

For the droplet flow regime, the interfacial heat transfer coefficient from the liquid side is calculated from [14]:

$$h_{i\ell,d} = \frac{2}{3}\pi^2 \frac{k_\ell}{d_e} \cdot 2.7 \tag{2.2.133}$$

Here $h_{i\ell,d}$ has been modified by a factor of 2.7 to include the effect of internal circulation in the droplet. For the vapor side, the interfacial heat transfer coefficient is given by [13]:

$$h_{ig,d} = \frac{k_g}{d_e} Nu_{g,d} \tag{2.2.134}$$

where:

$$Nu_{g,d} = 2 + 0.74\sqrt{\frac{\rho_g d_e v_{rd}}{\mu_g}} Pr_g^{1/3} \tag{2.2.135}$$

2.2.5.3.3 *Annular Flow*

For films, the interfacial heat transfer coefficients for the vapor and liquid sides are given by [13]:

$$h_{ig,f} = 0.02\ \rho_g v_f C_{p,g} \tag{2.2.136}$$

and

$$h_{i\ell,f} = 0.02\ \rho_\ell v_f C_{p,\ell} \tag{2.2.137}$$

where:

$$v_f = \frac{\delta g \Delta\rho}{3\mu_\ell}$$

is the film velocity derived from a simple force balance on a falling film, assuming viscous flow and a linear velocity distribution in the film.

In the transition flow regime, the heat transfer coefficient and the interfacial area are obtained from interpolation of the corresponding values in the bubbly/churn and the annular drop flow regimes with respect to α to provide smooth transition from liquid continuous to vapor continuous flow regime.

2.2.6 Turbulent Mixing

2.2.6.1 Mixing Mechanism

During turbulent flow, portions of fluids are exchanged laterally among adjacent sub channels leading to transport of mass, momentum and energy. These effects alter axial mass flux, quality, void fraction and enthalpy distribution in the sub channels.

The two-phase mixing process illustrated in Figure 2-2 assumes equal volume exchange of two-phase mixtures (eddies) brought about by the turbulence of the flow field.

The lateral transport rates are functions of cross–flow area, lateral mixing velocities and fluid properties of the participating sub channels. The cross flow area in a rod bundle is typically much larger than the axial flow area in a subchannel node. Thus even for small mixing velocities the lateral exchange rates may be significant compared to the axial flow rates. This puts considerable emphasis on evaluating the mixing velocity accurately.

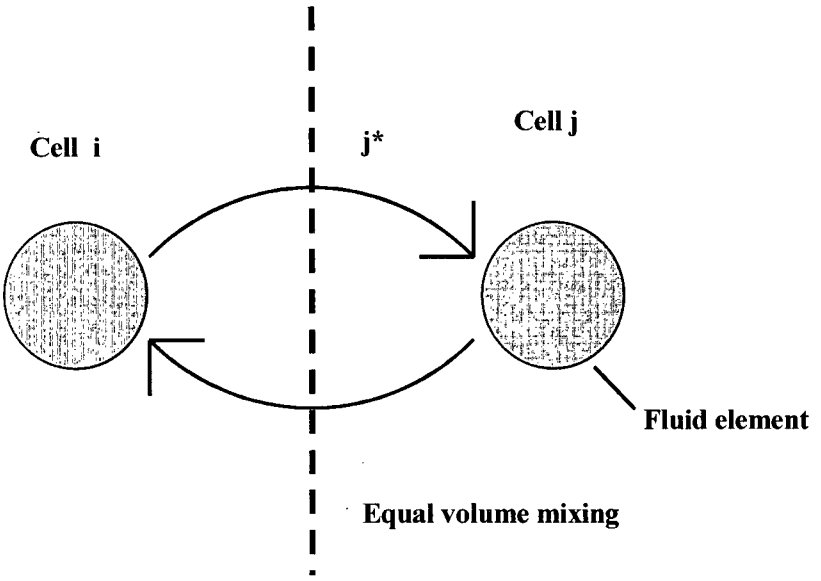

Figure 2-2. Turbulent Mixing in Two-Phase Mixture

2.2.6.2 Modeling Approach

[[

]]

2.2.6.3 Formulation of Mixing Rates

[[

(2.2.138)

(2.2.139)

]](2.2.140)

2.2.6.4 Correlations

2.2.6.4.1 *Single Phase Mixing*

[[

(2.2.141)

(2.2.142)

(2.2.143)

(2.2.144)

(2.2.145)

(2.2.146)

]]

For bubbly flow, liquid is the continuous phase, and for annular flow, vapor is the continuous phase.

2.2.6.4.2 *Two -Phase Multiplier*

[[

(2.2.147)

(2.2.148)

(2.2.149)

(2.2.150)

(2.2.151)

]]

2.2.6.4.3 *Mixing at High Steam Qualities*

[[

(2.2.152)

(2.2.153)

(2.2.154)

(2.2.155)

(2.2.156)

(2.2.157)

(2.2.158)

(2.2.159)

(2.2.160)

(2.2.161)

]](2.2.162)

2.2.6.5 Mixing Enhancements Due to Spacers and Flow Tabs

Spacers and flow tabs produce increase in fluid mixing by generating increased turbulence. These mixing enhancement effects are described in Section 3.1.

2.2.7 Void Drift

It has been observed from experiments [21], that vapor tends to migrate toward regions with high mass flux or high turbulent kinetic energy. For a BWR fuel bundle this phenomenon will cause the vapor to migrate from the corner and side sub channels toward the central subchannel generating a region in the center of the bundle with high mass flux and void fraction. This migration cannot be explained by pressure drop driven cross flow between the sub channels, and a separate void–drift model is needed to account for this phenomenon.

Past void–drift models [19] have traditionally been rather empirical. A typical example on such model can be expressed as:

$$\alpha_{oi} - \alpha_{oj} = k\left(G_i - G_j\right) \tag{2.2.163}$$

where α_o is the equilibrium void fraction corresponding to the mass flux distribution.

[[

]]

Figure 2-3. Void-Drift Model

[[

(2.2.164)

(2.2.165)

(2.2.166)

(2.2.167)

(2.2.168)

(2.2.169)

]]

2.2.8 Entrainment

2.2.8.1 Entrainment Mechanisms

In annular two-phase flow, a fraction of liquid flowing along the surface is converted to droplets in the gas/vapor core. Hewitt [22] postulates three possible mechanisms: 1) entrainment due to bursting of bubbles at a heated surface having a liquid film, 2) undercutting of the liquid film by breakdown of disturbance waves, 3) entrainment due to breakdown of disturbance wave due to "rolling" action.

2.2.8.2 Modeling Approach

There are two-inherent issues to modeling droplet entrainment for reactor applications. The first is the inception of entrainment and the second is the rate of entrainment.

2.2.8.2.1 *Inception of Entrainment*

In vertical up flow through tubes and sub channels, the flow regimes may include transitions from single-phase flow to two-phase bubbly flow to churn-turbulent flow, leading to fully developed annular flow. Studies in low pressure air-water systems by Kataoka and Ishii [23] indicate that (1) entrainment inception occurs when the local liquid film Reynolds number exceeds a value of 160, (2) the axial distance required to achieve equilibrium entrainment varies directly as the axial distance, inversely as the hydraulic diameter, is proportional to the square root of the total liquid Reynolds number and is inversely proportional to the fourth-root of the droplet Weber number. These entrainment inception data are quite limited in range to be used for entrainment calculations for high pressure steam water systems.

An alternative modeling approach chosen here assumes entrainment inception when void fraction reaches the critical void fraction for transition to annular flow.

2.2.8.2.2 *Rate of Entrainment*

The approach described here is based on the phenomena of roll wave entrainment. The resulting formulation and correlation will more accurately describe the available steam-water data over a range of conditions (pressure, mass flux, hydraulic diameter, etc.) typical of BWRs. The correlation is flexible enough to be modified and applied to valuable separate effects film flow data in low pressure air–water test facilities thus providing additional confirmation of the entrainment mechanism assumed above.

2.2.8.3 Formulation for Shear on Liquid Film

In annular flow the vapor-droplet core moves at a faster rate than the liquid film. This results in exchange of momentum at the film-core boundary which produces interfacial shear.

When the shear is large enough, wave motion is induced in the liquid film. For very large shear the amplitude of these waves, measured in terms of sand roughness or wave height, may be up to an order of magnitude larger than the mean film thickness.

[[

(2.2.170)

(2.2.171)

(2.2.172)

]]

2.2.8.4 Correlations

2.2.8.4.1 *Interfacial Friction Factor*

[[

(2.2.173)

]](2.2.174)

2.2.8.4.2 *Liquid Film Roughness*

[[

(2.2.175)

]]

2.2.8.4.3 *Entrainment Rate*

[[

(2.2.176)

]](2.2.177)

2.2.8.5 Entrainment from Spacers, Trippers and Part Length Rods

Transfer of liquid from the film to the core occurs in presence of spacers, trippers and part length rods.

Enhanced droplet entrainment occurs upstream of the spacer (1) due to increased shear and (2) due to obstruction of the film flow by spacer hardware. These effects are described in Section 3.1.

Flow trippers intercept the film flow along the channel wall promoting entrainment and increasing the availability of the channel wall water to the rods. These effects are discussed in Section 3.3.

All of the liquid flowing as film along the part length rod has to be entrained as droplets at the upper end of the rod. The modeling of this phenomenon is discussed in Section 3.2.

2.2.9 Deposition

2.2.9.1 Deposition Mechanisms

In published literature two descriptions of the droplet deposition process have been incorporated into mathematical models for annular two–phase flow.

The first description assumes the droplet deposition to be a mass transfer process. Also, the droplet flux depositing on the liquid film is assumed proportional to the mean droplet concentration in the gas core. The "constant" of proportionality is termed as the Mass Transfer Coefficient:

$$G_d = k\,C \qquad (2.2.178)$$

where G_d is the deposition mass flux referred to unit surface area of the film, k is the mass transfer coefficient having units of velocity, and C is the droplet concentration in the vapor–droplet core.

Whalley [26] proposed an empirical correlation of the mass transfer coefficient k in terms of surface tension only. Based on burnout studies using steam-water flow in vertical tubular geometry, Bennett [27] suggested that the mass transfer coefficient is likely to depend on vapor quality and droplet concentration in the gas core.

The second description of deposition is due to Hutchinson, et al., [28] and assumes that the droplets in the gas core interact with turbulent eddies such that the deposition process is diffusive.

Bennett [27] suggested that the deposition coefficient k might be thought of as a lateral drift velocity of the droplets towards the liquid film surface. He indicated that the turbulence in the gas phase affects this velocity. Furthermore, the droplet concentration affects this 'drift' velocity in two ways. Firstly, at high droplet concentration, droplets will coalesce and respond less to the turbulence of the vapor stream. Secondly, turbulence itself is damped by increasing droplet concentration. Both effects are in the same direction tending to decrease the 'drift' velocity and, hence substantially decrease the deposition coefficient k at low steam qualities.

Bennett suggested that in the presence of turbulence the deposition coefficient may be functionally represented as

$$k = f\left(G_g, C\right) \tag{2.2.179}$$

where G_g is the mass flux and C droplet concentration in the vapor-droplet core region.

Sugawara [29] invoked the similarity of heat and mass transfer in turbulent flow to provide a description of the deposition coefficient k in terms of droplet concentration, gas Reynolds number and Schmidt number.

2.2.9.2 Modeling Approach

[[

]]

where the mass fluxes are based on the cross-sectional flow area of the vapor–droplet core.

2.2.9.3 Formulation

2.2.9.3.1 *Deposition Coefficient*

[[

(2.2.180)

(2.2.181)

(2.2.182)

]]

2.2.9.3.2 *Droplet Concentration*

[[

]](2.2.183)

2.2.9.4 Deposition Correlation

[[

(2.2.184)

]]

2.2.9.5 Deposition on Spacers and Flow Tabs

The enhancement of droplet deposition due to spacers and flow tabs are described in Section 3.1. The flow tabs are treated similar to the spacer for this specific enhancement.

2.2.9.6 Film Spreading

[[

(2.2.185)

(2.2.186)

]]

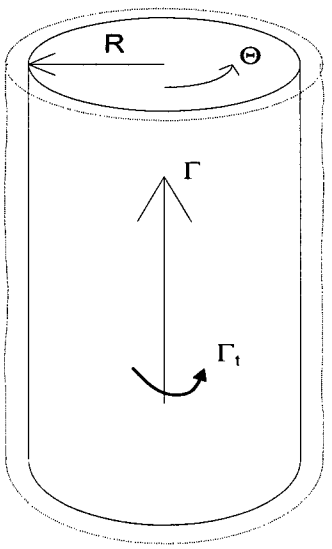

Figure 2-4. Film Spreading

3.0 HARDWARE MODELS

3.1 Spacer

COBRAG is mainly used to predict critical power for BWR fuels through a detailed description of the liquid film dynamics and a critical film thickness prediction on the heated surface. The liquid film dynamics include the processes of entrainment, deposition, and film evaporation. The hardware such as BWR fuel spacers alters the rate of deposition and entrainment through altering the flow field. COBRAG allows a detailed description of such processes by a semi-empirical approach for modeling of flow features in downstream and upstream of the spacers.

3.1.1 Objectives

The main objectives of the spacer model development task are:

- Develop semi–empirical spacer thermal hydraulics model
- Develop models applicable to multi–dimensional, single–phase and two–phase conditions
- Develop models applicable to BWR pressure and mass flux conditions
- Develop models applicable to egg crate, ferrule and advanced product line spacers
- Develop models applicable for trend study of significant design and operational variables
  - number of spacers in the bundle; spacer pitch
  - lattice dimensions; rod dimensions; dimensions of spacer elements
  - axial and radial power profile
  - mass flux; subcooling; pressure

The qualification of the spacer model is demonstrated by the qualification of COBRAG against ATLAS critical power data [30]

3.1.2 Approach

The modeling is based on the following approach:

- Capture major physical phenomena upstream and downstream of a spacer
- Focus on alteration of flows of droplet, liquid film, and steam by spacer
- Focus on separate treatment of multiple liquid films in a single fluid–centered subchannel
- Simplify modeling by adopting "projected area" principles (e.g., drag coefficient, droplet collection)

3.1.3 Classification of Spacer Effects

[[

-

]]

3.1.4 Physical Models

3.1.4.1 Droplet Deposition Enhancement (Downstream Effect)

[[

(3.1.1)

(3.1.2)

(3.1.3)

]]

Figure 3-1. Droplet Deposition Enhancement Downstream of a Spacer

3.1.4.1.1 *Evaluation of the Droplet Deposition Enhancement Factor*

[[

(3.1.4)

]]

3.1.4.1.2 *Specification of Background Fluctuation Velocity*

[[

(3.1.5)

(3.1.6)

(3.1.7)

]]

3.1.4.1.3 *The Equivalent Friction Coefficient (f_{eq})*

[[

(3.1.8)

(3.1.9)

(3.1.10)

(3.1.11)

(3.1.12)

(3.1.13)

(3.1.14)

(3.1.15)

(3.1.16)

(3.1.17)

(3.1.18)

]]

3.1.4.1.4 *Specification of* u_{rs} *(fluctuation velocity in the wake)*

[[

(3.1.19)

]]

3.1.4.1.5 *The near field downstream of the spacer*

[[

]]

Figure 3-1 shows that the outer edge of the near field is at a distance Z1 from the element. Schlichting [33] provides analytical results for diffusivity in the wake region immediately behind the single body:

[[(3.1.20)

(3.1.21)

]](3.1.22)

3.1.4.1.6 *The far field (eddy diffusivity in the wake behind a row of cylinders)*

[[

]]

Figure 3-2. Schematic Of Flow Patterns Behind A Row Of Bars

[[(3.1.23)

(3.1.24)

(3.1.25)

(3.1.26)

(3.1.27)

(3.1.28)

(3.1.29)

(3.1.30)

]]

3.1.4.1.7 *Determination of the Boundary of the Near Field and the Far Field*

[[

]](3.1.31)

3.1.4.1.8 *Local Value of Spacer Downstream Deposition Enhancement Factor*

[[

(3.1.32)

(3.1.33)

]]

3.1.4.1.9 *The Integrated Average Enhancement Factor*

[[

(3.1.34)

(3.1.35)

(3.1.36)

]]

3.1.4.2 Turbulent Mixing Enhancement (Downstream Effect)

[[

]]

Figure 3-3. Turbulent Mixing Enhancement from Droplet Deposition Enhancement

[[

(3.1.37)

(3.1.38)

]]

3.1.5 Liquid Film Shear Enhancement (Upstream Effect)

[[

]]

Figure 3-4. Shear and Entrainment Enhancement Upstream of a Spacer

[[

(3.1.39)

(3.1.40)

(3.1.41)

(3.1.42)

(3.1.43)

(3.1.44)

(3.1.45)

(3.1.46)

(3.1.47)

(3.1.48)

(3.1.49)

(3.1.50)

(3.1.51)

(3.1.52)

(3.1.53)

(3.1.54)

(3.1.55)

]]

3.1.5.1 Entrainment Enhancement from Obstructions and Contacts (Upstream Effect)

[[

]]

Figure 3-5. Entrainment Enhancement Upstream of a Spacer Due to Liquid Film Cutoff by Contacts

[[(3.1.56)

(3.1.57)

]]

3.1.5.2 Droplet Collection by Spacer Hardware and Liquid Runoff (Upstream Effect)

[[

]]

Figure 3-6. Schematic of Droplet Collection and Liquid Runoff at a Spacer

[[

(3.1.58)

(3.1.59)

(3.1.60)

]](3.1.61)

3.1.5.3 Spacer Irreversible Pressure Drop

[[

]]

3.1.5.3.1 *The* $K-\varphi_{\ell o}^2$ *model for two–phase pressure drop multiplier (single change of flow area).*

[[

(3.1.62)

]]

3.1.5.3.2 *The φ_c^2 two–phase multiplier model (expansion-contraction combination: Long Insert Model).*

[[

]](3.1.63)

The expression for the two-phase multiplier for the expansion-contraction passages in spacer elements, φ_c^2 is given in Section 2.2.3 under wall friction and singular losses.

3.2 Part Length Rod

The geometry and power generation of the part length rod are modeled through the input specifications. The following effects downstream of the part length rod are considered:

[[

]]

3.3 Flow Tripper

Flow trippers are grooves in the channel wall that entrain liquid films and make relatively more liquid available to the fuel rods.

3.3.1 Mechanism

The flow tripper model is based on the following assumptions:

[[

]]

3.3.2 Physical Model

[[

(3.1.64)

]]

4.0 NUMERICAL METHOD

4.1 Discretization of Thermal Hydraulic Equations

In this section the finite-difference form of the conservation equations resulting from discretization will be presented. The finite-difference equations are written in a semi-implicit form with donor cell differencing for convective quantities and based on a staggered computational cell shown in .

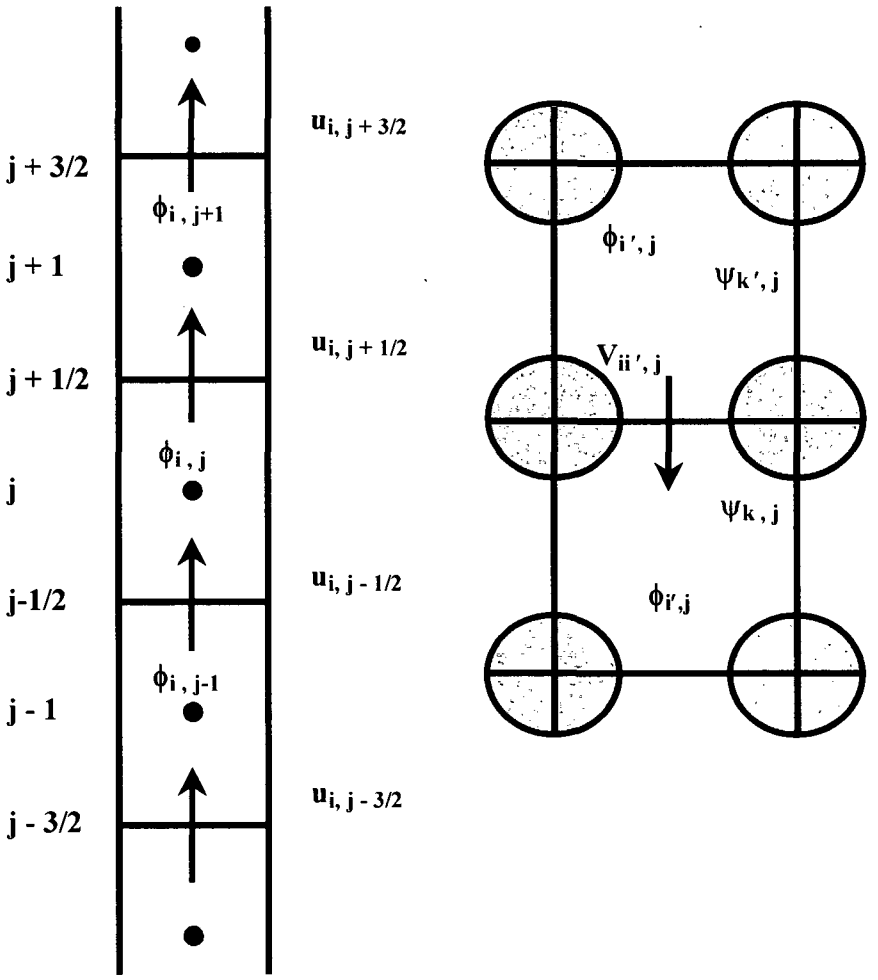

Figure 4-1. Staggered Grid Variables

Mass Conservation Equations

Vapor mass:

$$V_{i,j}\left\{(\alpha_g\rho_g)^{n+1}_{i,j} - (\alpha_g\rho_g)^{n}_{i,j}\right\} = \Delta t\, A_{i,j-\frac{1}{2}}\, u^{n+1}_{g\,i,j-\frac{1}{2}}\,(\alpha_g\rho_g)^{d}_{i,j-\frac{1}{2}}$$
$$\Delta t\, A_{i,j+\frac{1}{2}}\, u^{n+1}_{g\,i,j-\frac{1}{2}}\,(\alpha_g\rho_g)^{d}_{i,j+\frac{1}{2}} + \Delta t \sum_{i'} A_{ii',j}\, v^{n+1}_{g\,ii',j}\,(\alpha_g\rho_g)^{d}_{ii',j} + \Delta t\, V_{i,j}(\Gamma^{n+1}_{g} + M^{n+1}_{mix,g})_{i,j} \tag{4.2.1}$$

Liquid mass:

$$V_{i,j}\left\{(\alpha_e\rho_\ell)^{n+1}_{i,j} - (\alpha_e\rho_\ell)^{n}_{i,j}\right\} = \Delta t\, A_{i,j-\frac{1}{2}}\, u^{n+1}_{e\,i,j-\frac{1}{2}}\,(\alpha_e\rho_\ell)^{d}_{i,j-\frac{1}{2}} - \Delta t\, A_{i,j+\frac{1}{2}}\, u^{n+1}_{e\,i,j+\frac{1}{2}}\,(\alpha_e\rho_\ell)^{d}_{i,j+\frac{1}{2}}$$
$$+ \Delta t \sum_{i'} A_{ii',j}\, v^{n+1}_{e\,ii',j}\,(\alpha_e\rho_\ell)^{d}_{ii',j} + \Delta t\, V_{i,j}(-\Gamma^{n+1}_{e} + M^{n+1}_{mix,e})_{i,j} + \Delta t\, V_{i,j} \sum_{k}\left(E^{n+1}_{k} - D^{n+1}_{k}\right)_{i,j} \tag{4.2.2}$$

Liquid film mass:

$$V_{i,j}\left\{(\alpha_f\rho_\ell)^{n+1}_{k,j} - (\alpha_f\rho_\ell)^{n}_{k,j}\right\} = \Delta t\, A_{i,j-\frac{1}{2}}\, u^{n+1}_{f\,k,j-\frac{1}{2}}\,(\alpha_f\rho_\ell)^{d}_{k,j-\frac{1}{2}} - \Delta t\, A_{i,j+\frac{1}{2}}\, u^{n+1}_{f\,k,j+\frac{1}{2}}\,(\alpha_f\rho_\ell)^{d}_{k,j+\frac{1}{2}}$$
$$+ \Delta t \sum_{k'} A_{kk',j}\, v^{n+1}_{f\,kk',j}\,(\alpha_f\rho_\ell)^{d}_{kk',j} + \Delta t\, V_{i,j}(-\Gamma^{n+1}_{f} + M^{n+1}_{f})_{k,j} - \Delta t\, V_{i,j}\left(E^{n+1}_{k,j} - D^{n+1}_{k,j}\right) \tag{4.2.3}$$
$$+ \Delta t\, V_{i,j} M^{n+1}_{fs\,k,j}$$

4.2 Momentum Conservation Equations

Vapor momentum – vertical direction:

$$u^{n+1}_{g\,i,j+\frac{1}{2}} - u^{n}_{g\,i,j+\frac{1}{2}} = -\Delta t\, u^{n}_{g\,i,j+\frac{1}{2}}\left(\frac{\partial u_g}{\partial z}\right)^{d}_{i,j+\frac{1}{2}} - \Delta t \sum_{i'} v^{n}_{g\,ii',j+\frac{1}{2}}\left(\frac{\partial u_g}{\partial x}\right)^{d}_{ii',j+\frac{1}{2}} - \Delta t \frac{P^{n+1}_{i,j+1} - P^{n+1}_{i,j}}{\rho^{n}_{g\,i,j+\frac{1}{2}}(z_{i+1} - z_i)}$$
$$- \Delta t g - \Delta t \frac{\left(F_{ie,z}\right)^{n+1}_{i,j+\frac{1}{2}}}{\left(\alpha_g\rho_g\right)^{n}_{i,j+\frac{1}{2}}} - \Delta t \sum_{k} \frac{\left(F_{if,z}\right)^{n+1}_{k,j+\frac{1}{2}}}{\left(\alpha_g\rho_g\right)^{n}_{i,j+\frac{1}{2}}} - \Delta t \sum_{k} \frac{\left(F_{wg,z}\right)^{n+1}_{k,j+\frac{1}{2}}}{\left(\alpha_g\rho_g\right)^{n}_{i,j+\frac{1}{2}}} + \Delta t \frac{\left(B_{mix,g}\right)^{n+1}_{i,j+\frac{1}{2}}}{\left(\alpha_g\rho_g\right)^{n}_{i,j+\frac{1}{2}}} \tag{4.2.4}$$

Vapor momentum – lateral direction:

$$v^{n+1}_{g\,ii',j} - v^{n}_{g\,ii',j} = -\Delta t\, v^{n}_{g\,ii',j}\left(\frac{\partial v_g}{\partial s}\right)^{d}_{ii',j} - \Delta t\, u^{n}_{g\,ii',j}\left(\frac{\partial v_g}{\partial z}\right)^{d}_{ii',j} - \Delta t \frac{P^{n+1}_{i,j} - P^{n+1}_{i',j}}{\rho^{n}_{g\,ii',j}\delta s_{ii',j}} - \Delta t \frac{\left(F_{wg,s}\right)^{n+1}_{ii',j}}{\left(\alpha_g\rho_g\right)^{n}_{ii',j}}$$
$$- \Delta t \frac{\left(F_{ie,s}\right)^{n+1}_{ii',j}}{\left(\alpha_g\rho_g\right)^{n}_{ii',j}} - \Delta t \frac{\left(F_{if,s}\right)^{n+1}_{ii',j}}{\left(\alpha_g\rho_g\right)^{n}_{ii',j}} + \Delta t \frac{\left(F_{vd,s}\right)^{n+1}_{ii',j}}{\left(\alpha_g\rho_g\right)^{n}_{ii',j}} \tag{4.2.5}$$

Liquid momentum – vertical direction:

$$u^{n+1}_{\ell i,j+\frac{1}{2}} - u^{n}_{\ell i,j+\frac{1}{2}} = -\Delta t\, u^{n}_{\ell i,j+\frac{1}{2}} \left(\frac{\partial u_\ell}{\partial z}\right)^{d}_{i,j+\frac{1}{2}} - \Delta t \sum_{i'} v^{n}_{\ell ii',j+\frac{1}{2}} \left(\frac{\partial u_\ell}{\partial x}\right)^{d}_{ii',j+\frac{1}{2}} - \Delta t \frac{P^{n+1}_{i,j+1} - P^{n+1}_{i,j}}{\rho^{n}_{\ell i,j+\frac{1}{2}} (z_{i+1} - z_i)} - \Delta t\, g$$
$$+ \Delta t \frac{\left(F_{ie,z}\right)^{n+1}_{i,j+\frac{1}{2}}}{\left(\alpha_\ell \rho_\ell\right)^{n}_{i,j+\frac{1}{2}}} - \Delta t \sum_{k} \frac{\left(F_{we,z}\right)^{n+1}_{k,j+\frac{1}{2}}}{\left(\alpha_\ell \rho_\ell\right)^{n}_{i,j+\frac{1}{2}}} + \Delta t \frac{\left(B_{mix,\ell}\right)^{n+1}_{i,j+\frac{1}{2}}}{\left(\alpha_\ell \rho_\ell\right)^{n}_{i,j+\frac{1}{2}}} + \Delta t \sum_{k} \frac{E^{n}_{k,j+\frac{1}{2}}}{\left(\alpha_\ell \rho_\ell\right)^{n}_{i,j+\frac{1}{2}}} \left(u^{n+1}_{fk,j+\frac{1}{2}} - u^{n+1}_{\ell i,j+\frac{1}{2}}\right) \quad (4.2.6)$$

Liquid momentum – lateral direction:

$$v^{n+1}_{\ell ii',j} - v^{n}_{\ell ii',j} = -\Delta t\, v^{n}_{\ell ii',j} \left(\frac{\partial v_\ell}{\partial s}\right)^{d}_{ii',j} - \Delta t\, u^{n}_{\ell ii',j} \left(\frac{\partial v_\ell}{\partial z}\right)^{d}_{ii',j} - \Delta t \frac{P^{n+1}_{i,j} - P^{n+1}_{i',j}}{\rho^{n}_{\ell ii',j} \delta s_{ii',j}} - \Delta t \frac{\left(F_{w\ell,s}\right)^{n+1}_{ii',j}}{\left(\alpha_\ell \rho_\ell\right)^{n}_{ii',j}}$$
$$+ \Delta t \frac{\left(F_{ie,s}\right)^{n+1}_{ii',j}}{\left(\alpha_\ell \rho_\ell\right)^{n}_{ii',j}} - \Delta t \frac{\left(F_{vd,s}\right)^{n+1}_{ii',j}}{\left(\alpha_\ell \rho_\ell\right)^{n}_{ii',j}} \quad (4.2.7)$$

Liquid film momentum – vertical direction:

$$u^{n+1}_{fk,j+\frac{1}{2}} - u^{n}_{fk,j+\frac{1}{2}} = -\Delta t\, u^{n}_{fk,j+\frac{1}{2}} \left(\frac{\partial u_f}{\partial z}\right)^{d}_{k,j+\frac{1}{2}} - \Delta t \sum_{i'} v^{n}_{fkk',j+\frac{1}{2}} \left(\frac{\partial u_f}{\partial x}\right)^{d}_{kk',j+\frac{1}{2}}$$
$$- \Delta t \frac{P^{n+1}_{i,j+1} - P^{n+1}_{i,j}}{\rho^{n}_{\ell i,j+\frac{1}{2}} (z_{i+1} - z_i)} - \Delta t\, g + \Delta t \frac{\left(F_{if,z}\right)^{n+1}_{k,j+\frac{1}{2}}}{\left(\alpha_f \rho_\ell\right)^{n}_{k,j+\frac{1}{2}}} - \Delta t \sum_{k} \frac{\left(F_{wf,z}\right)^{n+1}_{k,j+\frac{1}{2}}}{\left(\alpha_f \rho_\ell\right)^{n}_{k,j+\frac{1}{2}}} \quad (4.2.8)$$
$$+ \Delta t \frac{\left(B_{fs}\right)^{n+1}_{k,j+\frac{1}{2}}}{\left(\alpha_\ell \rho_\ell\right)^{n}_{k,j+\frac{1}{2}}} - \Delta t \sum_{k} \frac{D^{n}_{k,j+\frac{1}{2}}}{\left(\alpha_\ell \rho_\ell\right)^{n}_{i,j+\frac{1}{2}}} \left(u^{n+1}_{fk,j+\frac{1}{2}} - u^{n+1}_{\ell i,j+\frac{1}{2}}\right)$$

Liquid film momentum – lateral direction:

$$v^{n+1}_{fkk',j} - v^{n}_{fkk',j} = -\Delta t\, v^{n}_{fkk',j} \left(\frac{\partial v_f}{\partial s}\right)^{d}_{kk',j} - \Delta t\, u^{n}_{fkk',j} \left(\frac{\partial v_f}{\partial z}\right)^{d}_{kk',j} - \Delta t \frac{P^{n+1}_{i,j} - P^{n+1}_{i',j+1}}{\rho^{n}_{\ell ii',j}\, \delta s_{ii',j}} - \Delta t \frac{\left(F_{wf,s}\right)^{n+1}_{kk',j}}{\left(\alpha_f \rho_\ell\right)^{n}_{kk',j}}$$
$$+ \Delta t \frac{\left(F_{if,s}\right)^{n+1}_{kk',j}}{\left(\alpha_f \rho_\ell\right)^{n}_{kk',j}} + \Delta t \frac{\left(B_{fs,s}\right)^{n+1}_{kk',j}}{\left(\alpha_f \rho_\ell\right)^{n}_{kk',j}} \quad (4.2.9)$$

4.3 Energy Conservation Equations

Vapor energy:

$$
\begin{aligned}
&V_{i,j}\left\{\left(\alpha_g\rho_g h_g\right)_{i,j}^{n+1}-\left(\alpha_g\rho_g h_g\right)_{i,j}^{n}\right\} = \Delta t\, A_{i,j-\frac{1}{2}}\, u_{g\,i,j-\frac{1}{2}}^{n+1}\left(\alpha_g\rho_g h_g\right)_{i,j-\frac{1}{2}}^{d}\\
&-\Delta t\, A_{i,j+\frac{1}{2}} u_{g\,i,j+\frac{1}{2}}^{n+1}\left(\alpha_g\rho_g h_g\right)_{i,j+\frac{1}{2}}^{d}+\Delta t\sum_{i'} A_{ii',j}\, v_{g\,ii',j}^{n+1}\left(\alpha_g\rho_g h_g\right)_{ii',j}^{d}\\
&+\Delta t\, V_{i,j}\left\{\left(\Gamma_g h_g\right)_{i,j}^{n+1}+\left(E_{mix,g}\right)_{i,j}^{n+1}\right\}+\Delta t\, V_{i,j} q'''^{\,n+1}_{ig\,k,j}+\Delta t\sum_{k} S_{k,j} q''^{\,n+1}_{wg\,k,j}\\
&+\Delta t\, V_{i,j}\alpha_{g\,i,j}^{n+1}\left(P_{i,j}^{n+1}-P_{i,j}^{n}\right)
\end{aligned}
\qquad (4.2.10)
$$

Total energy:

$$
\begin{aligned}
&V_{i,j}\left\{h_{total\,i,j}^{n+1}-h_{total\,i,j}^{n}\right\}=\Delta t\, A_{i,j-\frac{1}{2}} u_{g\,i,j-\frac{1}{2}}^{n+1}\left(\alpha_g\rho_g h_g\right)_{i,j-\frac{1}{2}}^{d}-\Delta t\, A_{i,j+\frac{1}{2}} u_{g\,i,j+\frac{1}{2}}^{n+1}\left(\alpha_g\rho_g h_g\right)_{i,j+\frac{1}{2}}^{d}\\
&+\Delta t\sum_{i'} A_{ii',j} v_{g\,ii',j}^{n+1}\left(\alpha_g\rho_g h_g\right)_{ii',j}^{d}+\Delta t\, A_{i,j-\frac{1}{2}} u_{\ell\,i,j-\frac{1}{2}}^{n+1}\left(\alpha_\ell\rho_\ell h_\ell\right)_{i,j-\frac{1}{2}}^{d}\\
&-\Delta t\, A_{i,j+\frac{1}{2}} u_{\ell\,i,j+\frac{1}{2}}^{n+1}\left(\alpha_\ell\rho_\ell h_\ell\right)_{i,j+\frac{1}{2}}^{d}+\Delta t\sum_{i'} A_{ii',j} v_{\ell\,ii',j}^{n+1}\left(\alpha_\ell\rho_\ell h_\ell\right)_{ii',j}^{d}\\
&+\Delta t\sum_{k} A_{i,j-\frac{1}{2}} u_{f\,k,j-\frac{1}{2}}^{n+1}\left(\alpha_f\rho_\ell h_\ell\right)_{k,j-\frac{1}{2}}^{d}-\Delta t\sum_{k} A_{i,j+\frac{1}{2}} u_{f\,k,j+\frac{1}{2}}^{n+1}\left(\alpha_f\rho_\ell h_\ell\right)_{k,j+\frac{1}{2}}^{d}\\
&+\Delta t\sum_{k}\sum_{k'} A_{ii',j} v_{f\,kk',j}^{n+1}\left(\alpha_f\rho_\ell h_\ell\right)_{kk',j}^{d}+\Delta t\, V_{i,j}\left(P_{i,j}^{n+1}-P_{i,j}^{n}\right)\\
&+\Delta t\, V_{i,j}\left(\left(E_{mix,g}\right)_{i,j}^{n+1}+\left(E_{mix,\ell}\right)_{i,j}^{n+1}\right)+\Delta t\, V_{i,j}\sum_{k} E_{fs\,k,j}^{n+1}+\Delta t\sum_{k} S_{k,j} q''^{\,n+1}_{w\,k,j}
\end{aligned}
\qquad (4.2.11)
$$

4.4 Numerical Method

In this section, the overall principle of the numerical method is presented.

COBRAG uses a fully implicit integration technique for the conservation equations. The predictor–corrector method used by TRACG [37] is adopted to solve the discretized equations in section 4.1. The main principle of the method is to obtain the solution in two steps. The first step, called the predictor step, is to linearize the discretized equations in time such that the time step size is not restricted by the Courant limit. However, conservation of mass, momentum and energy are not maintained in this step. The second step, called the corrector step, is designed to restore the conservation.

4.4.1 Predictor Step

The predictor step linearizes the discretized equations in time such that the time step size is not restricted by the Courant limit.

4.4.1.1 Momentum Equations

The convective terms in the momentum equations uses the new time properties for outflow and old time properties for inflow. The shears, mixing, void drift, entrainment and

deposition are based on new velocities and approximated by Taylor expansion around old velocities. These equations constitute a set of linear equations in new velocities and new pressures. Consequently, the new velocities can be solved as function of the new pressures and are used to eliminate the velocities in the mass and energy equations.

4.4.1.2 Mass and Energy Equations

Similar to the momentum equations, the convective terms in the mass and energy equations use the new properties from the previous iteration for outflow and old time properties for inflow. The heat transfers, mixing, void drift, entrainment, deposition and evaporation and are based on the new properties. The mass and energy equations form a set of non-linear matrix equations in pressure, void fractions and temperatures that can be solved by any standard matrix inversion algorithm.

4.4.2 Corrector Step

Since conservation of properties is not maintained in the predictor step, the corrector step is to restore the conservation.

5.0 NOMENCLATURE

The following is a general list of symbols used in this document. Most symbols are defined where they appear in each section. SI units are used everywhere in this report.

5.1 Thermodynamic

C_p	constant pressure specific heat
e	specific internal energy
h	enthalpy
k	thermal conductivity
P	pressure
T	temperature

5.2 Thermal Hydraulic

A	flow area
$B_{mix,(e,g)}$	Momentum exchange due to the lateral turbulent mixing C_D drag coefficient
C_0	distribution parameter
c_f	interfacial friction factor
$C_{p,\ell}$	liquid Specific heat at constant pressure
d	diameter
D_h	hydraulic diameter
D_k	Liquid deposition rate on to film k
E_k	Liquid entrainment rate from film k
$E_{mix,(g,e)}$	Energy increase due to mixing
$E_{fs,k}$	Energy increase due to film spreading
f	friction factor or force per unit volume
$\vec{F}_{ie}$	Interfacial shear between liquid in the core and vapor
$\vec{F}_{if,k}$	Interfacial shear between vapor and film k
$\vec{F}_{wg,k}$	Wall shear stress acting on vapor by surface k
$\vec{F}_{vd}$	Void drift force
$\vec{F}_{we,k}$	Wall friction acting on liquid in the core by surface k
g	acceleration due to gravity
G	mass flux
H	heat transfer coefficient
j	volumetric flux

$M_{mix,(e,g)}$	Mass gain due to lateral mixing
$q_{wg,k}$	Energy input rate through surface k to vapor
q_{ig}	Energy Transfer rate to vapor from interface
$q_{w,k}$	Energy addition from surface k
q''	heat flux
q'''	volumetric heat generation rate
R_e	Reynolds Number
Pe	Peclet number
u_{rs}	fluctuation velocity in the wake
v_{rb}	bubble relative velocity
$\bar{v}_{gj}$	cross-sectional average vapor drift velocity
V	volume
W	mass flow rate
x	quality
x_c	Core quality
ΔP_c	Singular Pressure Drop

5.3 Superscripts

$\rightarrow$	vector quantity

5.4 Subscripts

b	bubble
c	continuous phase, condensation, or critical
CHF	critical heat flux
d	donor cell property
e	droplet
f	liquid film
g	vapor
ℓ	liquid
i	interface
ii'	gap index
ld	liquid departure
m	mixture
min	minimum
w	wall
vd	void drift

5.5 Greek

α	void fraction
Γ_g	volumetric vapor generation rate
Γ_e	volumetric liquid generation rate
$\Gamma_{f,k}$	volumetric liquid film generation rate
ε	surface roughness, eddy diffusivity
ρ	density
$\rho_{2\varphi}$	homogeneous two-phase mixture density
χ_{tt}	Martinelli parameter
μ	viscosity
σ	surface tension or Stephan-Boltzman constant
τ	shear stress
Φ_{lo}	two-phase multiplier
θ_{mix}	the two-phase turbulent mixing multiplier

5.6 Special Notation

ΔX	change in quantity
δX	increment or differential change
$\langle X \rangle$	Surface average quantity

6.0 REFERENCES

1. C. L. Wheeler, et al., "COBRA–NC: A Thermal–Hydraulic Code for Transient Analysis of Nuclear Reactor Components," NUREG/CR–3262, PNL–5515, Pacific Northwest Laboratory, May 1986.
2. J. G. M. Andersen, et al., "TRACG Qualification – Licensing Topical Report", NEDE–32177P, February 1993.
3. M. Ishii, "One Dimensional Drift–Flux Model and Constitutive Equations for Relative Motion Between Phases in Various Two–Phase Flow Regimes", ANL–77–47, October 1977.
4. Y. Taitel, D. Borvea and A. E. Dukler, "Modeling Flow Pattern Transitions for Steady Upward Gas–Liquid Flow in Vertical Tubes", AICHE Journal, No. 3, pp. 345–354, 1980.
5. J. A. Findlay and G. E. Dix, "New BWR Void Fraction Correlation", General Electric Company, NEDE–21565, January 1977.
6. J. Waggener, "Friction Factors for Pressure Drop Calculations", Nucleonics, Vol. 19, (No. 11), November 1961.
7. J. G. M. Andersen, K. H. Chu. and J. C. Shaug, "BWR REFILL/REFLOOD Program TASK 4.7 - Model Development, Basic Models for the BWR Version of TRAC", GEAP–22051, NUREG/CR–2573, EPRI NP–2375, April 1983.
8. W. T. Hancox and W. B. Nicoll, "Prediction of Time–Dependent Diabatic Two–Phase Water Flows", Progress in Heat and Mass Transfer, Vol. 6 Pergamon Press, pp 119–135 1972.
9. N. Zuber and J. A. Findlay, "Average Volumetric Concentration in Two Phase Flow Systems", Journal of Heat Transfer, 87, p. 453, 1965.
10. N. Zuber, et al., "Steady State and Transient Void Fraction in Two-Phase Flow Systems", GEAP-5417, 1967.
11. J. Nikuradse, "Gesetzmasigkeit der Turbulenten Stromung–in glatten Rohren", Forch. Arb. Ing. Wes, p. 356, 1932.
12. G. B. Wallis, "One Dimensional Two–Phase Flow," McGraw–Hill Book Co., Inc., New York, 1969.
13. R. J. Pryor, et al., "TRAC–P1A, An Advanced Best Estimate Computer Program for PWR LOCA Analysis", Los Alamos Scientific Laboratory, NUREG/CRA–0665, LA–777–7S, May, 1979.
14. J. G .M. Andersen and H. Abel–Larsen, "CORECOOL–Model Description of the Programme", Department of Reactor Technology, Riso National Laboratory, Denmark, RISO–M–21380, November 1980.
15. J. T. Rogers and R. G. Rosehart, "Mixing by Turbulent Interchange in Fuel Bundles, Correlations and Inferences," ASME, 72-HT-53, (1972).

16. D. S. Rowe and C. W. Angle, "Cross Flow Mixing Between Parallel Flow Channels During Boiling, BNWL-371, Battelle Northwest Laboratories, 1967.

17. M. S. Kazimi, and J. E. Kelly, "Formulation of a Two-Fluid Model for Mixing in LWR Bundles," Thermal Hydraulics of Nuclear Reactors (Edited by Mati Merilo, EPRI), Volume I, pp. 433-439, American Nuclear Society, 1983. (Collection of Papers Presented at the Second International Meeting on Nuclear Reactor Thermal Hydraulics, Santa Barbara, California, January 11-14, 1983.

18. E. Bergles, et al., "Two-Phase Flow and Heat Transfer in the Power and Process Industries", (pp. 142-145", Singular Pressure Drops by J. M. Delhaye), Hemisphere Publishing Corporation, New York, 1981.

19. J. M. Gonzalez and R. W. Radcliffe, "MIXER2 -- A Digital Computer Program for Steady State Subchannel Analysis and CHF Prediction," NEDE 13240, August 1972.

20. Mohammed Abolfadl and Graham B. Wallis, "An Improved Mixing Length Model for Annular Two-Phase Flow with Liquid Entrainment," Nuclear Engineering and Design, 95 (1986), pp. 233-241.

21. R. T. Lahey, B. S. Shiralkar, and D. W. Radcliffe, "Two–Phase Flow and Heat Transfer in Multirod Geometries: Subchannel and Pressure Drop Measurements in a Nine–rod Bundle for Diabatic and Adiabatic Conditions," GEAP–13049, March 1970.

22. G. F. Hewitt and N. S. Hall–Taylor, "Annular Two–Phase Flow," pp. 136-138, First Edition, 1970, Pergamon Press, New York.

23. I. Kataoka and M. Ishii, "Entrainment Rate in Annular Two–Phase Flow," ANL/RAS/LWR 82–1, Argonne National Laboratory, February 1982.

24. L. M. Hossfeld, D. Bharathan, G. B. Wallis, and H. J. Richter, "Interfacial Friction in Co–current Upward Annular Flow," EPRI NP2326, 1982.

25. Jørgen Würtz, "An Experimental and Theoretical Investigation of Annular Steam Water Flow in Tubes and Annuli at 30 to 90 Bar," RISØ Report No. 372, RISØ National Laboratory, Denmark, April, 1978.

26. P. B. Whalley, "The Calculation of Dryout in a Rod Bundle," International Journal of Multiphase Flow, Vol. 3, No. 6-A, 1977, pp. 505-515.

27. W. Bennett, G. F. Hewitt, H. A. Kersey, and R. K. F. Keeys, "Experiments on Burnout in a Uniformly Heated Round Tube at 1000 psia with Steam–Water Mixtures at the Tube Inlet," AERE–R 5072, Harwell, England, 1965.

28. P. Hutchinson, G. F. Hewitt, and A. E. Dukler, "Deposition of Liquid or Solid Dispersion from Turbulent Gas Streams: A Stochastic Model," Chem. Eng. Sci., Vol. 26, 1971, pp 419-439.

29. Satoru Sugawara, "Droplet Deposition and Entrainment Modeling Based on the Three Fluid Model,", Third International Topical Meeting on Nuclear Power Plant Thermal Hydraulics and Operations, (Proceedings), November, 1988, Seoul, Korea, pp. A1-19 to A1-28.

30. GEXL14 correlation for GE14 fuel, NEDC-32851P, Rev. 2, September 2001.

31. Akio Tomiyama and Osamu Yokomizo, "Spacer Effects on Film Flow in BWR Fuel Bundle", Journal of Nuclear Science and Technology, pp. 204-206, Feb. 1988.

32. J. O. Hinze, Turbulence, p. 726, McGraw-Hill, Second Edition, 1975.

33. H. Schlichting, Boundary Layer Theory, McGraw-Hill, Fourth Edition, pp. 590-605.

34. W. M. Kays, "Convective Heat and Mass Transfer", p.71, McGraw–Hill, 1966.

35. Toshio Aihara and Wu-Shung Fu, "Effects of Droplet Size Distribution and Gas Phase Flow Separation upon Inertia Collection of Droplets by Bluff Bodies in Gas-Liquid Mist Flow", International Journal of Multiphase Flow, Vol. 12, No. 3, pp. 389-403, 1986.

36. J. Weisman, A. Hussain, and B. Harshe, "Two-Phase Pressure Drop Across Abrupt Area Changes and Restrictions," Two-Phase Transport and Reactor Safety, Volume IV (Proceedings of the Two-Phase Flow and Heat Transfer Symposium Workshop, October 18-20, 1976, Florida), Hemisphere Publishing Corporation, Washington.

37. J. Waggener, "Friction Factors for Pressure Drop Calculation", Nucleonics, 19 (11), November 1961.